# Magnetic anisotropy in the near-stoichiometric van der Waals ferromagnet $Fe_3GeTe_2$

Riju Pal,[1,2,3,*] Joyal John Abraham,[1,2] Satyabrata Bera,[4] Mintu Mondal,[4] Atindra Nath Pal,[3] Bernd Büchner,[1,2,5] Vladislav Kataev,[1] and Alexey Alfonsov[1,†]

[1]*Leibniz Institute for Solid State and Materials Research, Helmholtzstrasse 20, D-01069 Dresden, Germany*

[2]*Institute for Solid State and Materials Physics, TU Dresden, D-01062 Dresden, Germany*

[3]*Department of Condensed Matter and Materials Physics, S. N. Bose National Centre for Basic Sciences, Block JD, Sector III, Salt Lake, Kolkata 700106, India*

[4]*School of Physical Sciences, Indian Association for the Cultivation of Science, Jadavpur, Kolkata 700032, India*

[5]*Institute for Solid State and Materials Physics and Würzburg-Dresden Cluster of Excellence ctd.qmat, TU Dresden, D-01069 Dresden, Germany*

(Received 27 April 2026; revised 14 October 2026; accepted 19 October 2026; published 17 November 2026)

Quasi-two-dimensional (2D) van der Waals (vdW) ferromagnets such as the series $Fe_{3-x}GeTe_2$, with a relatively high Curie temperature and robust metallicity, offer an ideal platform for investigating itinerant magnetism in reduced dimensions. Here, we present a comprehensive electron spin resonance (ESR) investigation of single-crystalline, almost stoichiometric $Fe_{3.03\pm0.03}GeTe_2$ across wide ranges of frequencies, temperatures, and magnetic fields to gain quantitative insights into its magnetic anisotropy and spin dynamics. Frequency-dependent ESR measurements establish $Fe_3GeTe_2$ as an easy-axis ferromagnet. Temperature-dependent high-field ESR reveals a large internal field that gradually decreases at higher temperatures. Remarkably, this internal field persists even above $T_C$, indicating short-range spin correlations in $Fe_3GeTe_2$. Analysis of spin-wave modes yields a strong uniaxial magnetocrystalline anisotropy $K_{int} \approx -5 \times 10^6$ erg cm$^{-3}$ at 3 K and a large magnon gap $\Delta(3\,\mathrm{K}) \approx 87.8 \pm 13.7$ GHz ($\approx 0.363 \pm 0.057$ meV). Our study highlights that small variations in Fe content in $Fe_3GeTe_2$ lead to substantial changes in the magnon gap at low temperatures, indicating the sensitivity of spin dynamics to the chemical composition. These results establish $Fe_3GeTe_2$ as a model vdW ferromagnet for exploring tunable anisotropies and magnon excitations in metallic 2D magnets.

DOI: 10.1103/27h2-qnt8

## I. INTRODUCTION

Layered vdW crystals comprise a versatile class of quantum materials that continue to attract significant attention due to their novel fundamental properties and technological potential [1,2]. Of particular interest are 2D magnetic vdW materials, which can retain long-range magnetic order even in the atomically thin limit, offering promising routes toward miniaturized magnetic memory and spintronic devices [3–5]. In such systems, the inherently weak interlayer vdW bonding renders many compounds effectively quasi-2D even in their bulk form, since strong intralayer exchange dominates over much weaker interlayer couplings. Additionally, magnetic anisotropy plays an important role in stabilizing the magnetic ground state and controlling the spin dynamics, even in the monolayer limit [6–8]. A quantitative understanding of such anisotropy is therefore essential for describing the microscopic origin and robustness of 2D magnetism and realizing novel spintronic functionalities. In this context, magnetic resonance methods, in particular high-frequency/high-field electron-spin-resonance (HF-ESR) technique, is a sensitive and direct probe of anisotropic fields, magnon excitation gaps, and the temperature dependence of spin relaxation, as well as overall spin dynamics in low-dimensional vdW magnets [9–19].

Following the experimental discovery of intrinsic 2D ferromagnetism in insulating compounds such as $CrI_3$ and $Cr_2Ge_2Te_6$ [20,21], numerous vdW magnets, including $CrBr_3$, $CrSiTe_3$, $FePS_3$, and $NiPS_3$, have been investigated [22–26], revealing unconventional electronic and magnetic properties. However, most of these materials are insulating or semiconducting, with their magnetic ordering temperatures being well below room temperature. In contrast, the $Fe_nGeTe_2$ family ($n \approx 3$–5) exhibits itinerant ferromagnetism with Curie temperatures ($T_C$) approaching or even exceeding room temperature [11,27–36], providing a promising platform for exploring 2D magnetism in metallic systems. $Fe_3GeTe_2$ is particularly notable due to its robust metallic ferromagnetism, strong uniaxial magnetic anisotropy, relative environmental stability, and thickness-dependent magnetic properties [37,38].

$Fe_3GeTe_2$ crystallizes in a hexagonal structure (space group $P6_3/mmc$), consisting of $Fe_3Ge$ layers sandwiched between two Te layers, where adjacent Te planes are held together by weak vdW forces [see Fig. 1(a)] [27,34,39,40]. The Fe sublattice contains two inequivalent crystallographic sites, commonly associated with $Fe^{3+}$ (Fe1) and $Fe^{2+}$ (Fe2). While both possess partially filled $d$ orbitals, theoretical studies

*Contact author: rijupal07@gmail.com

†Contact author: a.alfonsov@ifw-dresden.de

*Published by the American Physical Society under the terms of the Creative Commons Attribution 4.0 International license. Further distribution of this work must maintain attribution to the author(s) and the published article's title, journal citation, and DOI.*

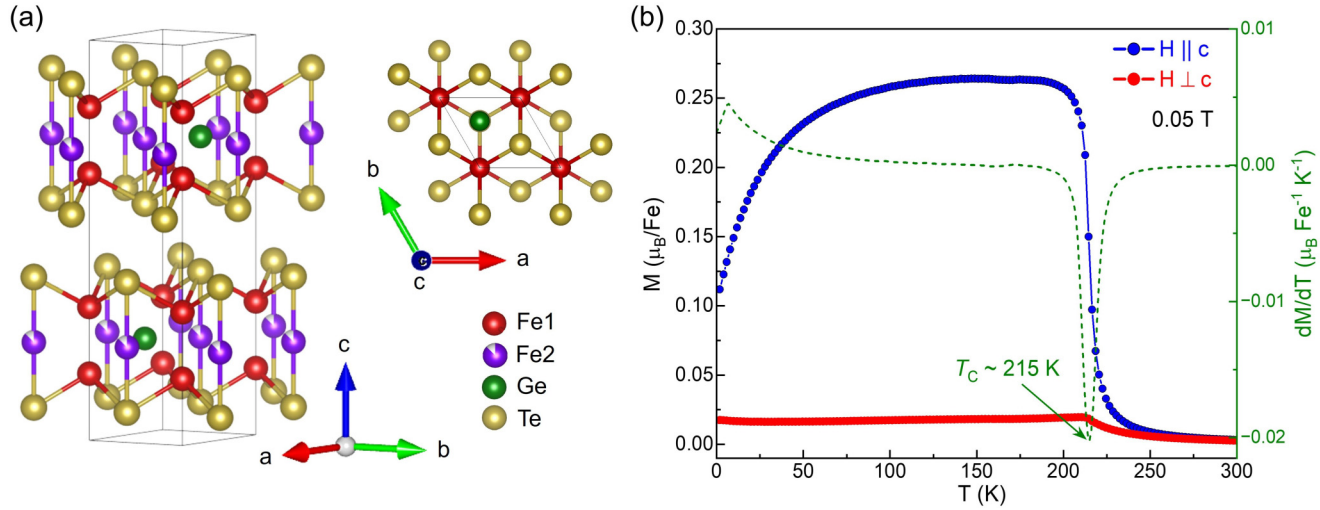



FIG. 1. (a) Crystal structure of $Fe_3GeTe_2$. The unit cell (left) and the top view (right) of a single vdW layer of $Fe_3GeTe_2$ are shown here. The unit cell is enclosed by the dotted lines. The top view of the structure shows the hexagonal symmetry of the *ab* plane. Two inequivalent Fe sites are termed Fe1 and Fe2. (b) The temperature dependence of magnetization and its temperature derivative, measured in zero-field-cooled (ZFC) condition under a magnetic field of 0.05 T (500 Oe) in the $\mathbf{H} \parallel \mathbf{c}$ and $\mathbf{H} \perp \mathbf{c}$ configurations. The minimum in the temperature derivative of the magnetization (dM/dT) for $\mathbf{H} \parallel \mathbf{c}$ reveals the Curie temperature $T_C \sim 215$ K of $Fe_3GeTe_2$.

indicate that they contribute differently to the magnetism: Fe1 generally hosts more localized moments, whereas Fe2 exhibits a more itinerant character, reflecting the mixed itinerant and localized nature of magnetism in this compound [41–43]. Bulk crystals exhibit a relatively high ferromagnetic ordering temperature ($T_C \approx 215$ K), with the magnetic easy axis aligned along the crystallographic *c* direction [Fig. 1(b)] [27,34]. Recent experiments have revealed a rich spectrum of correlated electronic and magnetic phenomena in the $Fe_3GeTe_2$ series, including a giant anomalous Hall effect [40,44], signatures of Kondo-lattice and heavy-fermion behavior [41], and topological spin textures such as skyrmions [45]. Moreover, its magnetic properties can be tuned by thickness [27,34,46], electrostatic gating [27], or strain [47,48], offering versatile control over its magnetic ground state. A particularly intriguing aspect of $Fe_3GeTe_2$ is its intrinsic nonstoichiometric nature. The Fe sublattice can accommodate vacancies in its Fe2 sites, leading to compositions commonly written as $Fe_{3-x}GeTe_2$, where even small variations in Fe occupancy significantly modify the magnetic moments, coercive fields, exchange interactions, and $T_C$ [49–52]. While the impact of Fe content on static magnetic properties is well established [50–52], its influence on magnon excitation gaps and magnetocrystalline anisotropy remains insufficiently understood. A recent study of a Fe-deficient crystal ($x = 0.08$) revealed markedly different spin-dynamic behavior [16], underscoring the exceptional sensitivity of this material to stoichiometry. A detailed investigation of the magnetic anisotropy and spin excitations in a near-stoichiometric $Fe_3GeTe_2$ is therefore crucial to elucidate the role of Fe stoichiometry in spin dynamics, particularly near the stoichiometric limit ($n \approx 3$), and to establish it as a key tuning parameter for controlling magnetic anisotropy and spin excitations within the $Fe_{3-x}GeTe_2$ family.

In this work, we present a comprehensive ESR investigation of single-crystalline $Fe_3GeTe_2$ with a near-stoichiometric, slightly Fe-rich composition (Fe content $\sim 3.03 \pm 0.03$) over wide ranges of frequency, temperature, and both in-plane and out-of-plane magnetic field orientations. HF-ESR measurements confirm $Fe_3GeTe_2$ as an easy-axis ferromagnet with a large anisotropy field of $\sim$3.2 T at 3 K, which remains mostly temperature-independent up to $\sim$100 K before gradually decreasing at higher temperatures. A finite shift of the ferromagnetic resonance lines persists even above $T_C$, indicating the presence of short-range spin correlations in $Fe_3GeTe_2$. The intrinsic uniaxial magnetocrystalline anisotropy energy reaches $\sim -5 \times 10^6$ erg cm$^{-3}$ at 3 K, yielding a sizable magnon excitation gap of $\Delta(3\text{ K}) \approx 87.8 \pm 13.7$ GHz ($\approx$0.363 $\pm$ 0.057 meV), comparatively large among vdW ferromagnets. Comparison with previously reported Fe-deficient compositions reveals pronounced variations in both anisotropy and magnon gap, highlighting the sensitivity of the anisotropy and spin dynamics in $Fe_3GeTe_2$ to its Fe content. Overall, these results demonstrate Fe stoichiometry as an effective microscopic control parameter for tuning magnetic anisotropy and magnon excitation gaps in the $Fe_{3-x}GeTe_2$ family, thereby positioning it as a model metallic vdW ferromagnet for engineering tunable spin excitations in low-dimensional magnetic systems.

## II. EXPERIMENTAL DETAILS

High-quality single crystals of $Fe_3GeTe_2$ were synthesized [53] following the conventional chemical vapor transport (CVT) method [34,39,54], using iodine ($I_2$) as the transport agent. A stoichiometric mixture of high-purity elemental powders of Fe, Ge, and Te (purity 99.99%) in a molar ratio of 3:1:2 was thoroughly ground using an agate mortar. Subsequently, $I_2$ powder was added at a concentration of 5 mg cm$^{-3}$, and the entire mixture was sealed in an evacuated quartz tube under a pressure of $2 \times 10^{-4}$ mbar. The sealed quartz tube was then placed horizontally in a two-zone tube furnace, where the

temperature was maintained at 750 °C on the source side and 700 °C on the growth side for a period of seven days. After the growth process, multiple high-quality, shiny, thin single crystals were obtained at the colder end, with typical dimensions around $2 \times 1.5 \times 0.1$ mm$^3$. Structural phase analysis was carried out on some of these crystals using x-ray diffraction (XRD) on a Rigaku diffractometer with Cu-$K_\alpha$ radiation ($\lambda = 1.54056$ Å), while micromorphology was examined via field emission scanning electron microscopy (FESEM, JEOL LSM-6500). Energy-dispersive x-ray spectroscopy (EDX) on the freshly cleaved surface of the measured bulk crystal confirms that it is nearly stoichiometric, slightly Fe-rich, with an average elemental composition of $Fe_{3.03(3)}Ge_{0.89(4)}Te_{2.00(1)}$ (see Fig. 7 in Appendix A). Although the Ge content is slightly below the ideal occupancy, there is no existing evidence that Ge deficiency plays a significant role in determining the magnetic properties of $Fe_3GeTe_2$ (see Appendix A). The synthesis procedure, along with detailed structural and physical characterizations confirming the high quality of the grown crystals, has been reported in the earlier work [53].

Temperature- and magnetic field-dependent magnetization measurements ($M-T$ and $M-H$) of the $Fe_3GeTe_2$ crystal were performed using a magnetic properties measurement system (MPMS-SQUID by Quantum Design, USA). The $M-T$ measurements were carried out in the temperature range of 1.8–300 K under an applied magnetic field of 0.05 T oriented both in the *ab* plane and along the *c* axis [see Fig. 1(b)]. To minimize the remanent or residual magnetization present in the sample, an external magnetic field of 5 T was applied at 300 K and then gradually reduced to zero while periodically changing the field's polarity. All measurements were conducted under zero-field-cooled (ZFC) conditions: The sample was cooled from 300 down to 1.8 K in the absence of an external field. Magnetization data were collected during the warming cycle under a constant applied field.

A well-characterized bulk single crystal of $Fe_3GeTe_2$, with dimensions approximately $1.74 \times 1.47 \times 0.24$ mm$^3$, was chosen for electron paramagnetic resonance (EPR) and ferromagnetic resonance (FMR) measurements. Conceptually, the primary distinction between EPR and FMR lies in the nature of their excitations: EPR probes the resonant excitation of individual paramagnetic spins, whereas FMR involves the collective excitations of the net magnetization (**M**) in a ferromagnetically ordered state [19,55]. Since the instruments used for the detection of both resonances are the same, in the text below, we will use a more general term, electron spin resonance (ESR). High-frequency and high-field (HF) ESR studies were conducted using a custom-built spectrometer. Microwaves (MW) in the frequency range of 75 to 330 GHz were generated and detected using the PNA-X vector network analyzer (Keysight Technologies) with frequency extensions from Virginia Diodes, Inc. (VDI), as well as with a set of amplifier multiplier chains (AMC) and zero-bias detectors (ZBD) also from VDI. Continuous magnetic field sweeps were performed using a superconducting magnet (Oxford Instruments). A home-made probehead equipped with oversized waveguides was inserted into a variable temperature insert (VTI) of a $He^4$ cryostat (Oxford Instruments), allowing the stabilization of sample temperature between 3 and 300 K. All the measurements were carried out by continuously sweeping the magnetic field from 0 to 16 T and back at fixed frequencies and temperatures. In the HF-ESR system, utilizing a vector network analyzer, some instrumental mixing of the absorption and dispersion signals is unavoidable due to the complex impedance of the broadband probehead. Since the spectral lines deviate from a Lorentzian shape, it was impossible to account for such a mixing during the fitting procedure; $H_{\rm res}$ and $\Delta H$ were determined by manual picking of the position of the minimum of the resonance line and by calculating the full width at half of this minimum, respectively. In order to extract these values $H_{\rm res}$ and $\Delta H$ from such a mixed signal at the detector, we employed the approach reported in [11].

## III. RESULTS AND DISCUSSION

### A. Frequency dependence of HF-ESR response

To investigate the magnetic anisotropies and *g* factors of $Fe_3GeTe_2$ in detail, we performed frequency-dependent ESR measurements at some selected temperatures—in the magnetically ordered state (at 3 and 100 K) and well above the magnetic phase transition (at 300 K) in both configurations of the magnetic field $\mathbf{H} \parallel \mathbf{c}$ and $\mathbf{H} \perp \mathbf{c}$. The corresponding frequency vs magnetic field ($\nu$-$H$) diagrams are presented in Figs. 2(a), 2(b), and Fig. 9 in Appendix B. Exemplary spectra are displayed on the right vertical axis of Fig. 2. At all temperatures, the ESR spectra exhibit a single, relatively broad resonance line, with an average full width at half maximum (FWHM) of approximately 1 T. To account for potential uncertainties in the extracted parameters due to the spectral quality, we have assigned maximum possible error bars equal to the average spectral linewidth ($\approx$ 1 T) for all temperatures (3, 100, and 300 K) in the $\nu$-$H$ diagrams. Furthermore, owing to the spectral quality and the broad ESR signals, a reliable quantitative determination of the linewidth and the associated intrinsic damping parameters was not possible. A quantitative estimation of the Gilbert damping would require systematic broadband frequency-dependent FMR linewidth measurements on well-controlled thin samples, such as molecular beam epitaxy-grown thin films or exfoliated thin flakes of $Fe_3GeTe_2$, where extrinsic broadening effects could be minimized [55–57].

The expected paramagnetic resonance position at a resonance field $H_{\rm res}^{\rm para}$ can be estimated from the following relation [58]:

$$h\nu = g\mu_{\rm B}\mu_0 H_{\rm res}^{\rm para}, \tag{1}$$

where $\nu$ is the microwave frequency, $h$ is Planck's constant, $g$ is the $g$ factor of the resonating spins, $\mu_0$ is the vacuum permeability, $\mu_{\rm B}$ is the Bohr magneton.

The analytical expressions of the spin wave energies for a uniaxial easy-axis ferromagnet are [17,59,60]

$$\mathbf{H} \parallel \mathbf{c}: \quad h\nu = g\mu_{\rm B}\mu_0(H + |H_a|) \tag{2.1}$$

$$\mathbf{H} \perp \mathbf{c}: \quad h\nu = g\mu_{\rm B}\mu_0\sqrt{H(H - |H_a|)} \text{ for } H \geqslant |H_a| \tag{2.2}$$

$$h\nu = g\mu_B\mu_0\sqrt{|H_a|^2 - H^2} \text{ for } H \leqslant |H_a|, \tag{2.3}$$

where $H_{\rm a}$ is the total magnetic anisotropy field.

At 300 K ($\sim$85 K above $T_{\rm C}$), a linear dependence of frequency on the resonance field is observed in the $\nu$-$H_{\rm res}$

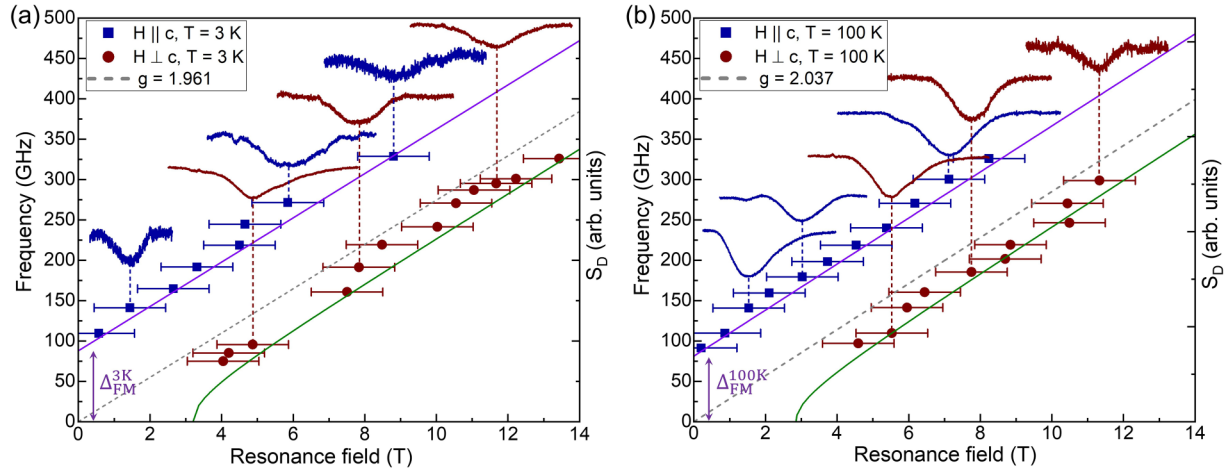



FIG. 2. Frequency dependence of the resonance fields $H_{\rm res}$ at $T = 3$ K (a) and 100 K (b) measured in $\mathbf{H} \parallel \mathbf{c}$ (blue squares) and in $\mathbf{H} \perp \mathbf{c}$ (red circles) configurations, respectively. Dashed lines represent the paramagnetic response estimated with Eq. (1) with the average $g$ factors given in the legends. Solid lines indicate the simulated best-fit results using Eqs. (2.1) and (2.2). Representative normalized and vertically shifted spectra are shown for some frequencies (right vertical axis), with colors indicating the respective magnetic-field orientations.

diagram for both field orientations (see Appendix B). This behavior is characteristic of the paramagnetic state of $Fe_3GeTe_2$ and can be described by the conventional paramagnetic resonance condition [see Eq. (1)]. Fits to the data according to Eq. (1) are shown in Fig. 9 in Appendix B as dashed lines, yielding an average expected paramagnetic $g = 2.07 \pm 0.04$.

In the magnetically ordered state at $T = 3$ K [see Fig. 2(a)], the resonance field data for $\mathbf{H} \parallel \mathbf{c}$ show a positive intercept on the frequency axis, suggesting a ferromagnetic behavior with a uniaxial easy-axis anisotropy. This magnetic anisotropy can also be associated with the presence of static internal fields on the ESR timescale, which shift the position of the ESR line. To determine the $g$ factors, unconstrained fitting of Eq. (2) to the measured data was used in this case. For $\mathbf{H} \parallel \mathbf{c}$, the fit using Eq. (2.1) yields $g_\parallel = 1.95 \pm 0.11$, whereas for $\mathbf{H} \perp \mathbf{c}$, $g_\perp = 1.97 \pm 0.06$. The average $g$ factor is thus $g_{\rm av}^{\rm 3K} \approx 1.96 \pm 0.08$. Now, using this averaged $g$ factor, the best-fit lines are calculated for $\mathbf{H} \perp \mathbf{c}$ and $\mathbf{H} \parallel \mathbf{c}$ simultaneously, based on a uniaxial easy-axis ferromagnet model [Eq. (2)]. These lines show good agreement with the experimental $\nu$-$H_{\rm res}$ data within the error bars [see Fig. 2(a)]. Therefore, at 3 K, the overall $\nu$-$H_{\rm res}$ dependence for both magnetic field orientations is found to be consistent with the expected behavior of a conventional uniaxial ferromagnet with easy-axis anisotropy and can be well described by Eqs. (2). The ferromagnetic zero-field magnon excitation gap ($\Delta$) for $\mathbf{H} \parallel c$, estimated from the intercept with the frequency axis, yields the value $\Delta_{\rm FM}|_{H=0} \equiv \Delta_{\rm FM}^{\rm 3K} \approx 87.8 \pm 13.7$ GHz ($\approx 0.363 \pm 0.057$ meV).

Similarly, at $T = 100$ K [Fig. 2(b)], the $\nu$-$H_{\rm res}$ dependence for both magnetic field orientations shows an easy-axis anisotropy. The best fit using Eqs. (2) provides $g_\parallel = 2.07 \pm 0.04$ for $\mathbf{H} \parallel \mathbf{c}$, and $g_\perp = 2.01 \pm 0.09$ for $\mathbf{H} \perp \mathbf{c}$. This results in an average $g$ factor $g_{\rm av}^{\rm 100\,K} \approx 2.04 \pm 0.07$. The estimated magnitude of the zero-field magnon excitation gap at $T = 100$ K is $\Delta_{\rm FM}^{\rm 100K} \approx 81.3 \pm 7.1$ GHz ($\approx 0.336 \pm 0.029$ meV), indicating a similar gap, within the error bar, to the value observed at $\sim 3$ K. Notably, this remarkably large and persistent magnon excitation gap in $Fe_3GeTe_2$, exceeding those reported for other vdW magnetic materials [11,18,23,61–67], underscores the strong magnetic anisotropy present in this system.

To examine the possible in-plane (*ab* plane) anisotropy, the $Fe_3GeTe_2$ crystal was rotated by 90° from its initial in-plane orientation (IP1). In this orthogonal in-plane configuration (IP2), the frequency dependence of the resonance field ($\nu$ vs $H_{\rm res}$) was measured at 3 and 100 K. A comparison between the results from the IP1 and IP2 configurations is presented in Fig. 10 in Appendix C. Within experimental uncertainty, both orientations yield nearly identical behavior at both temperatures, indicating the absence of measurable in-plane anisotropy in this $Fe_3GeTe_2$ sample. This observation is consistent with earlier findings from magnetization studies [40].

### B. Temperature dependence of HF-ESR response

The temperature evolution of the HF-ESR response in $Fe_3GeTe_2$ was investigated over the range $T = 3 - 300$ K at excitation frequencies close to 300 GHz for both magnetic field orientations, $\mathbf{H} \parallel \mathbf{c}$ and $\mathbf{H} \perp \mathbf{c}$. The corresponding ESR spectra are presented in Figs. 3(a) and 3(b), respectively. The vertical solid line indicates the expected paramagnetic resonance position ($H_{\rm res}^{\rm para}$), as determined from Eq. (1) using the $g$ factor measured at 300 K.

At the lowest measured temperature, the ESR responses are observed at magnetic fields either lower ($\mathbf{H} \parallel \mathbf{c}$) or higher ($\mathbf{H} \perp \mathbf{c}$) than the expected paramagnetic resonance position, respectively. This is in line with frequency-dependent measurements (see Sec. III A). As the temperature increases, for both magnetic field configurations, the resonance lines are gradually shifting toward the expected paramagnetic resonance line (see Fig. 3). To obtain a deeper understanding of how the magnetic anisotropy evolves with temperature, the resonance fields $H_{\rm res}$ and their temperature-dependent shifts, defined as $\delta H(T) = H_{\rm res}(T) - H_{\rm res}(300\,{\rm K})$, are plotted for both $\mathbf{H} \parallel \mathbf{c}$ and $\mathbf{H} \perp \mathbf{c}$ configurations as shown in Fig. 11 in Appendix D and Fig. 3(c), respectively. The reference resonance field, $H_{\rm res}(300\ {\rm K})$, was determined using Eq. (1), with

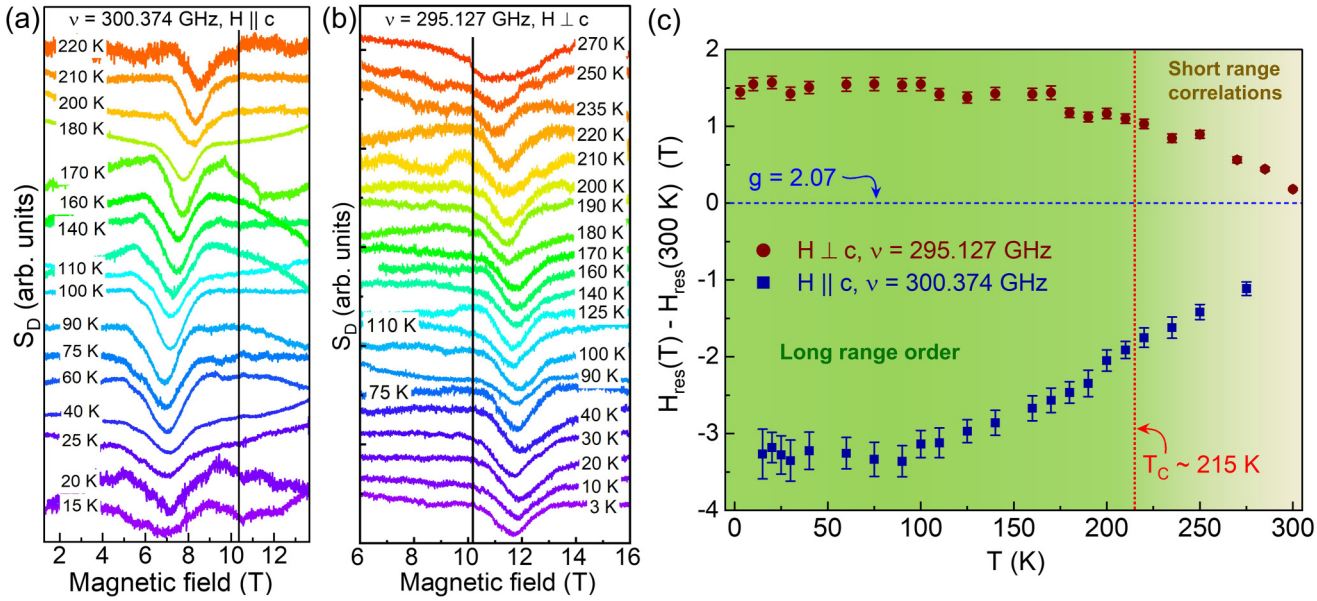



FIG. 3. Temperature evolution of the HF-ESR spectra in the field direction $\mathbf{H} \parallel \mathbf{c}$ (a) and $\mathbf{H} \perp \mathbf{c}$ (b), measured at fixed excitation frequencies of approximately 300 GHz. For clarity, all spectra are normalized to unity and vertically offset. Vertical black solid lines indicate the expected paramagnetic resonance position as given by Eq. (1). (c) Temperature dependence of the resonance shift, $\delta H(T)$, at a microwave frequency $\nu$ of $\approx 300$ GHz with an external magnetic field applied parallel (blue squares) and perpendicular (red circles) to the $c$ axis. A blue dashed line indicates the zero shift in the paramagnetic state with the $g$ factor, $g = 2.07$. The red dotted line shows the ordering temperature ($T_C \approx 215$ K) of $Fe_3GeTe_2$, determined at an applied magnetic field of 0.05 T. The color gradient illustrates the regions of long-range ordering and short-range correlations.

the $g$-factor value extracted from the $\nu$-$H_{res}$ data measured at $T = 300$ K. This shift $\delta H(T)$ serves as a measure of the deviation of the resonance field from the expected paramagnetic resonance position at each temperature. As depicted in Fig. 3(c), the $\delta H(T)$ dependence for two magnetic field orientations displays an asymmetric behavior relative to the zero-shift ($g = 2.07$) line. In general, the resonance shifts are more pronounced when the magnetic field is applied along the direction of the magnetic anisotropy axis—here along the $c$ axis of the $Fe_3GeTe_2$ crystal, as also reflected in Fig. 2. This observation highlights the $c$ axis as the dominant magnetic easy axis at all temperatures, aligning with the magnetization data (see Fig. 12 in Appendix E) [34,40,46].

Notably, the resonance shift [$\delta H(T)$] remains finite for both field orientations even at temperatures up to $\sim 300$ K [Fig. 3(c)], approximately 85 K above the $T_C \approx 215$ K of $Fe_3GeTe_2$, determined at an applied magnetic field of 0.05 T. We observed a pronounced enhancement of ferromagnetism with increasing external magnetic field [49] (see Fig. 13 in Appendix F): For fields above 0.5 T, $T_C$ increases monotonically, reaching $\sim$245 K at 7 T and can be extrapolated to $T_C \approx 255$ K at 10 T. As shown in Fig. 13 in Appendix F, the ferromagnetic phase transition at this field is broadened over a region of $\pm$ 25 K. The HF-ESR data shown in Fig. 3(c) were obtained at magnetic fields of $\sim$10 T, suggesting that the observed resonance shift up to $\sim$255 K arises from magnetic field-assisted enhancement of ferromagnetic correlations. However, a finite resonance shift persists up to room temperature ($\sim$300 K). This behavior indicates the possible presence of short-range spin correlations in $Fe_3GeTe_2$ that survive beyond the bulk ordering temperature. In quasi-2D vdW magnetic systems, weak interlayer coupling combined with strong magnetic anisotropy can stabilize short-range correlated spin regions over a finite temperature range above $T_C$. Within these regions, exchange interactions between neighboring spins generate finite local exchange fields. When these local fields fluctuate slowly compared with the HF-ESR timescale ($\sim$ 10 ps), they act as quasistatic internal fields for the resonating spins and modify the effective magnetic field experienced by the spins, resulting in the observed ESR line shift. Similar behavior has been reported in low-dimensional spin systems, where enhanced spin fluctuations and magnetic anisotropy allow magnetic correlations to persist well above the bulk ordering temperature [17,66,68,69].

### C. Estimation of the temperature dependence of magnetic anisotropy

To determine the temperature evolution of the total magnetic anisotropy field $H_a$, the temperature dependence of $H_{res}$ measured at $\approx 300$ GHz for both $\mathbf{H} \parallel \mathbf{c}$ and $\mathbf{H} \perp \mathbf{c}$ configurations was analyzed using Eqs. (2.1) and (2.2), respectively (see Fig. 11 in Appendix D). In this process, the $g$ factor was fixed at the paramagnetic value of $g \approx 2.07$. Consequently, the $H_a$ parameter was extracted, and its temperature evolution is presented in Fig. 4(a) for both magnetic field orientations. Here, the negative sign of $H_a$ defines the easy-axis type of anisotropy in $Fe_3GeTe_2$. As expected for uniaxial ferromagnets [Eq. (2)], the values of $H_a$ obtained for both $\mathbf{H} \parallel \mathbf{c}$ and $\mathbf{H} \perp \mathbf{c}$ are found to be practically the same at all temperatures. As can be seen in Fig. 4(a), $H_a$ is gradually increasing with decreasing temperature, and it becomes almost constant below $\sim$100 K within the error bars. Importantly, the values obtained here are consistent, within the experimental uncer-

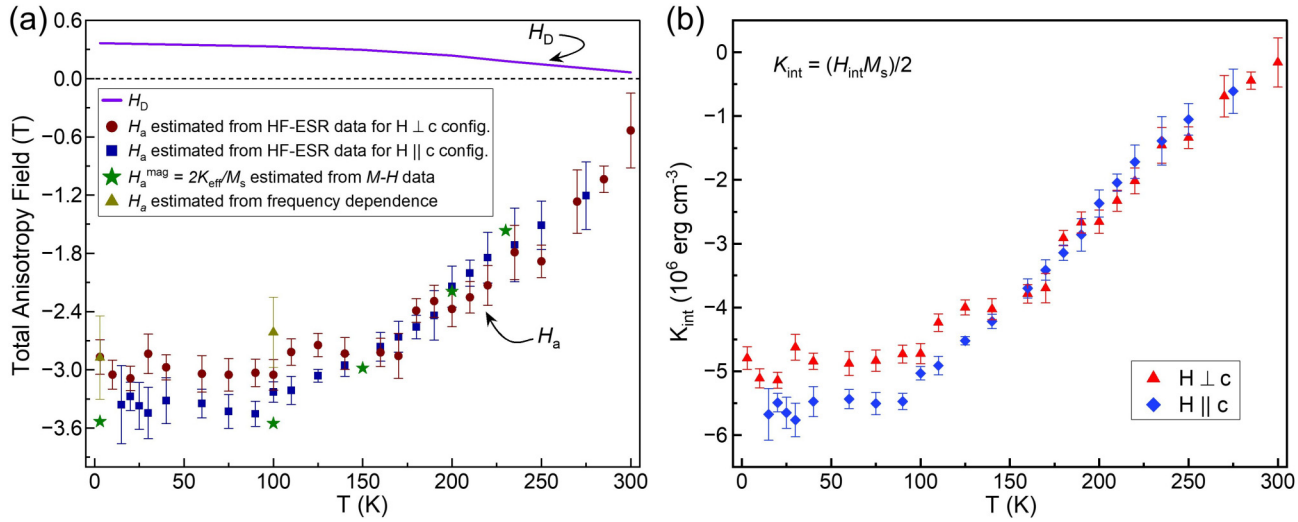



FIG. 4. (a) Total anisotropy field ($H_a$) as a function of temperature for both $\mathbf{H} \perp \mathbf{c}$ and $\mathbf{H} \parallel \mathbf{c}$ configurations, extracted from the temperature dependence of the resonance fields. The purple solid line is the calculated shape anisotropy field ($H_D$) given by the shape of the crystal. Green stars are the total anisotropy field calculated from the $M - H$ data. Yellow triangles are the total anisotropy field estimated from the frequency dependence of resonance fields at 3 and 100 K. (b) Temperature dependence of the intrinsic MA constant ($K_{int}$) estimated from the measurements in the $\mathbf{H} \perp \mathbf{c}$ and $\mathbf{H} \parallel \mathbf{c}$ configurations, respectively.

tainties, with the independent estimates of $H_a$ extracted from the frequency dependence of the resonance fields at 3 and 100 K (Fig. 2), as indicated in Fig. 4(a). This suggests that, even if fixing the $g$ factor to its paramagnetic value introduces a small deviation in the estimated $H_a$, it does not exceed the present experimental uncertainty. For comparison, $H_a$ values independently estimated from static magnetization ($M - H$) measurements at several selected temperatures are also included in Fig. 4(a) as star symbols and show reasonable agreement with the HF-ESR results (see Appendix G and Fig. 15 in Appendix H for more details). Furthermore, a previous study reported a magnetization-derived magnetic anisotropy energy of $\approx 3.8 \times 10^6$ to $0.4 \times 10^6$ erg cm$^{-3}$ over 2 to 205 K temperature ranges [36], which is also consistent with the effective magnetic anisotropy energy obtained from both our magnetization and HF-ESR measurements (see Fig. 15 in Appendix H).

To gain a deeper understanding of the magnetic anisotropy in $Fe_3GeTe_2$, it is essential to disentangle and quantify the intrinsic contribution from the total anisotropy by eliminating the extrinsic effect arising from the sample shape. The total anisotropy field at each temperature, obtained from the HF-ESR measurements, can then be expressed as the sum of two components [11]:

$$H_a = H_{\text{int}} + H_{\text{D}}, \tag{3}$$

where $H_{\text{int}}$ is the intrinsic magnetocrystalline anisotropy field. The term $H_{\text{D}}$ corresponds to the shape anisotropy field, which arises due to the sample geometry. This contribution can be quantitatively described by

$$H_{\text{D}} = 4\pi N M_{\text{s}}, \tag{4}$$

with $N$ representing the demagnetization factor for the platelike geometry of the sample, and $M_{\text{s}}$ denoting the saturation magnetization.

To investigate the origin of the total anisotropy field, the shape anisotropy field was first estimated at various temperatures. Considering the platelike shape of the sample with dimensions $1.74 \times 1.47 \times 0.24$ mm$^3$, the demagnetization factor was approximated as $N \approx 0.76$ for the measured crystal [70,71]. The shape anisotropy field ($H_{\text{D}}$) was then calculated using Eq. (4) with the saturation magnetization values $M_{\text{s}}(T)$ measured at different temperatures (see Fig. 16 in Appendix I). The result is plotted as a solid line in Fig. 4(a) and Fig. 17(a) in Appendix J. This estimate of $H_D$ enables determination of the intrinsic magnetocrystalline anisotropy field $H_{\text{int}}$ using Eq. (3).

The estimated $H_{\text{int}}$ is negative over the entire measurement temperature range (see Fig. 17(b) in Appendix J), confirming that the intrinsic magnetocrystalline anisotropy of $Fe_3GeTe_2$ is of the easy-axis type. Furthermore, the magnitude of $H_{\text{int}}$ is significantly larger than that of $H_D$ at all temperatures. Finally, the intrinsic magnetocrystalline anisotropy constant $K_{\text{int}} = H_{\text{int}}M_{\text{s}}/2$ was evaluated for both magnetic field orientations and is presented in Fig. 4(b). At 3 K, the value of $K_{\text{int}}$ reaches $\approx -5 \times 10^6$ erg cm$^{-3}$, which is nearly a factor of two smaller than that reported for the closely related compound with lower Fe content (= 2.92) [16], and yet remains significantly larger than the values reported for several other vdW ferromagnetic materials [see Fig. 6(a)] [11,18,23,61–67].

To visualize the magnetic anisotropy of a single sublattice in $Fe_3GeTe_2$, we can express the anisotropy energy density of a uniaxial ferromagnet whose easy axis lies along the crystallographic $c$ axis (taken as the $z$ axis) in polar coordinates as [7,8,72]

$$E_{\text{ani}} = K_u \cos^2\theta, \tag{5}$$

where $K_u < 0$ corresponds to *easy-axis* anisotropy and $\theta$ is the polar angle between the magnetization and the $z$ axis. For $K_u < 0$, the energy is minimized at $\theta = 0$ or $\pi$ ($E_{\text{ani}} = K_u$), corresponding to magnetization along $\pm z$ directions. In con-

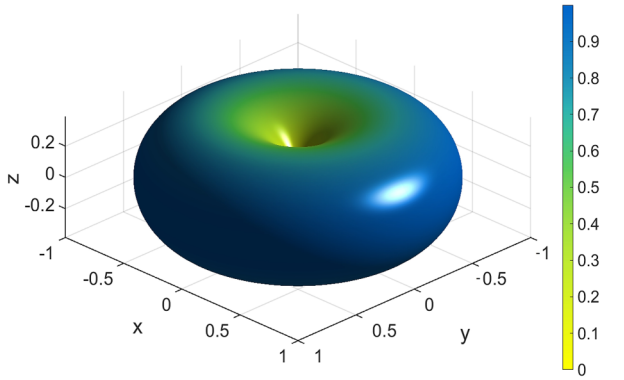



FIG. 5. Anisotropy energy density demonstration in Cartesian coordinates [following Eq. (5)], illustrating magnetic anisotropy of a single sublattice of $Fe_3GeTe_2$, as follows from the analysis of the HF-ESR results. Here, the yellow color corresponds to the energetically favorable direction (easy axis along the $c$ axis), while blue indicates higher-energy regions (hard plane). The surface is rotationally symmetric about the $z$ axis, reflecting the uniaxial magnetic anisotropy of the crystal.

trast, the energy is maximized at $\theta = \pi/2$ ($E_{\text{ani}} = 0$), i.e., when the magnetization lies in the $xy$ plane. Thus, the $\pm z$ direction defines the easy axis, while the $xy$ plane represents the hard-axis orientations. The energy difference between the hard- and easy-axis configurations is therefore $-K_u = |K_u|$. For $Fe_3GeTe_2$, the intrinsic magnetocrystalline anisotropy constant $K_{\text{int}}$ corresponds to $K_u$ and follows the same sign convention, with $K_{\text{int}} < 0$ denoting uniaxial easy-axis anisotropy throughout the measured temperature range.

Figure 5 illustrates the three-dimensional (3D) anisotropy energy density following Eq. (5). The color scale represents the magnitude of the anisotropy energy, with the yellow regions indicating the lowest-energy configurations (the easy axis along the $z$ direction) and blue regions corresponding to higher-energy orientations (along the $xy$ plane). The surface is rotationally symmetric about the $z$ axis, reflecting the uniaxial symmetry of the crystal: All azimuthal directions in the basal plane are energetically equivalent. This visualization highlights the easy-axis anisotropy and orientation dependence of the magnetization in $Fe_3GeTe_2$, consistent with its layered structure and spin-orbit-induced anisotropy [73,74].

As seen from Fig. 4(b), with increasing temperature, $K_{\text{int}}$ remains nearly constant up to $\approx 100$ K within the error bars, and then decreases rapidly at higher temperatures. Several studies on $Fe_{3-x}GeTe_2$ series have reported a temperature-driven reconstruction of its nontrivial electronic band structure below $T_C$, giving rise to significant electronic correlation effects, electron mass-renormalization, Fermi surface enlargement, and even a gradual formation of Kondo-lattice below $T^* \sim 100$ K [27,41,69,76–79], possibly related to the coexistence and complex interplay between localized moments and itinerant electrons occupying different $3d$ orbitals of Fe atoms in this metallic ferromagnet [41,69,77]. Such weakening of the temperature dependence of magnetocrystalline anisotropy energy density $K_{\text{int}}$ below $\sim 100$ K [see Fig. 4(b)] might be related to these electronic phenomena. Therefore, this finding calls for density functional theory (DFT) calculations, including spin-orbit coupling and Hubbard potential $U$, to obtain deeper insights into a possible influence of the observed electronic correlation effects on magnetocrystalline anisotropy.

To enable a direct comparison of the magnon excitation gap and intrinsic magnetocrystalline anisotropy energy of $Fe_3GeTe_2$ with those of other vdW ferromagnets measured at different temperatures, we evaluate the ferromagnetic zero-field magnon gap from our HF-ESR data. As the magnon gap is a manifestation of the out-of-plane magnetic anisotropy, it can be approximately estimated from the temperature dependence of the total anisotropy field $H_a$ for the $\mathbf{H} \parallel \mathbf{c}$ configuration [Fig. 4(a)] using Eq. (2.1) as

$$\Delta(T) = \nu|_{H=0} = \frac{g\mu_B\mu_0}{h}|H_a(T)|. \tag{6}$$

At $T = 15$ K, the zero-field magnon gap is estimated as $\Delta|_{15\,\text{K}} = 97.4 \pm 11.7$ GHz ($\approx 0.403 \pm 0.045$ meV). This large gap remains almost constant up to temperatures of approximately 100 K and agrees, within error bars, with the value obtained from the $\nu$-$H$ data at the same temperatures (Fig. 2). A comparison of the estimated magnon excitation gap and intrinsic magnetocrystalline anisotropy energy of different vdW ferromagnetic materials is plotted in Fig. 6(a).

Importantly, in the $Fe_nGeTe_2$ family, a close examination reveals that the zero-field magnon excitation gap is highly sensitive to the Fe content ($n$), particularly in the vicinity of $n \approx 3$. A comparison across different Fe compositions shows that the magnon gap decreases sharply with increasing Fe occupancy, as plotted in Fig. 6(b). For instance, the gap reduces from $\sim$895 GHz for $n = 2.75$ [68] to $\sim$230 GHz ($n = 2.86$) [75], $\sim$170 GHz ($n = 2.92$) [16], and further to $\sim$88 GHz for the near-stoichiometric, slightly Fe-rich composition ($n = 3.03 \pm 0.03$) investigated in the present work. This decreasing trend continues for higher members of the series, reaching $\sim$30.6 and 15 GHz for $n = 4$ [11], 20.6 GHz for $n = 4.73$ [61], and $\sim$6.4 GHz for $n = 5$ [18]. The magnon gap values compiled in Fig. 6(b) were obtained using different experimental techniques, including inelastic neutron scattering, magnetization, and FMR/HF-ESR measurements [11,16,18,61,68,75]. Since these techniques probe the spin excitations in different ways, some method-dependent variation in the absolute gap values cannot be excluded. For example, FMR/HF-ESR probes the uniform $q \approx 0$ mode, whereas inelastic neutron scattering determines the gap from the low-$q$ spin-wave dispersion. Therefore, Fig. 6(b) should be viewed as illustrating the overall evolution of the magnon gap with Fe content, with different symbols used to distinguish the corresponding experimental techniques.

In contrast, the Curie temperature $T_C$ exhibits a markedly different behavior, increasing nearly linearly with increasing Fe content [50,51], from $\sim$150 K at $n = 2.75$ to $\sim$215–217 K near $n \approx 3$, and further to $\sim$270 K ($n = 4$), $\sim$282 K ($n = 4.73$) and $\sim$332 K ($n = 5$) [11,16,18,61,68,75,80]. These results underscore the nontrivial and inverse relationship between different magnetic properties in $Fe_nGeTe_2$, establishing Fe stoichiometry as a crucial microscopic control parameter governing spin excitations.

A possible microscopic origin of this strong composition dependence near $n \simeq 3$ may lie in the pronounced sensitivity of the electronic structure and magnetic properties to Fe occupancy. In $Fe_{3-x}GeTe_2$, Fe deficiency occurs

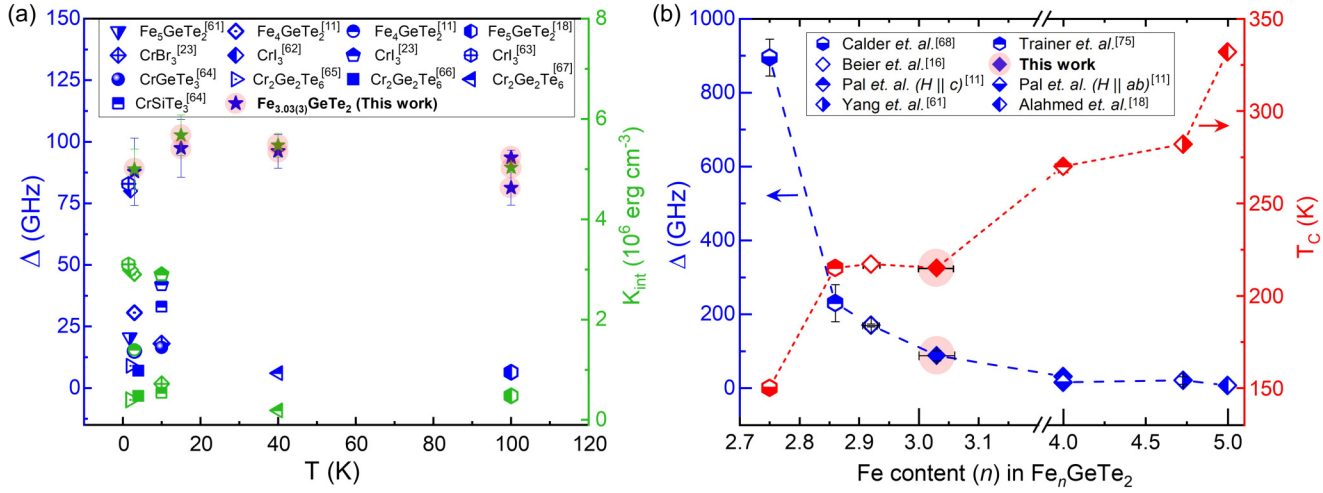



FIG. 6. (a) Comparison of zero-field magnon excitation gap (left axis and blue symbols) and intrinsic magnetocrystalline anisotropy energy (right axis and green symbols) of the measured $Fe_{3.03(3)}GeTe_2$ crystal (close to stoichiometric $Fe_3GeTe_2$) with those of other vdW ferromagnetic materials. The star symbol represents the values obtained from frequency- and temperature-dependent resonance field data in the present work. Data for the other materials are compiled from Refs. [11,18,23,61–67]. (b) Zero-field magnon excitation gap (left axis with blue symbols) and the ferromagnetic ordering temperature (right axis with red symbols) as a function of the Fe content in the $Fe_nGeTe_2$ family. The magnon gap exhibits a strong sensitivity to the Fe content, particularly near $n \approx 3$, where it decreases rapidly with increasing Fe occupancy. In contrast, $T_C$ increases nearly linearly with $n$. In addition to the present work (indicated by the highlighted solid diamond symbol), data for different Fe contents are taken from inelastic neutron scattering (indicated by the half-filled hexagon symbols) and FMR measurements (indicated by the diamond symbols) reported in Refs. [11,16,18,61,68,75].

predominantly at the Fe2 site, and changes in Fe2 occupancy are accompanied by variations in the lattice parameters, magnetic interactions, magnetic anisotropy, and $T_C$ [50–52,68,81]. Angle-resolved photoemission spectroscopy (ARPES), DFT, and DFT + DMFT studies indicate that Fe-deficiency-induced hole doping modifies the electronic structure near the Fermi level, shifts the chemical potential, thereby affecting the spin-orbit coupling-mediated contribution to the magnetocrystalline anisotropy [42,82,83]. Moreover, a recent work attributes the anomalous temperature dependence of the anisotropy to a complex competition between the two-ion mechanism and the itinerant-electron mechanism [79]. Thus, the magnetic anisotropy of $Fe_3GeTe_2$ may involve multiple microscopic contributions rather than a single mechanism. Importantly, ARPES, scanning tunneling microscopy/spectroscopy (STM/STS), inelastic neutron scattering, and theoretical studies have identified a complex coexistence of localized and itinerant Fe-3$d$ magnetism in $Fe_{3-x}GeTe_2$ [41,69,76,78,79]. DFT + DMFT calculations further revealed a pronounced site dependence, with Fe1 exhibiting a more persistent local-moment character and Fe2 showing a stronger tendency toward itinerant behavior [42,43,84]. At the same time, orbital-resolved calculations indicate that the Fe2 $d_{z^2}$ orbital itself plays an important role in local-moment formation [69,76]. Thus, changes in Fe occupancy may alter the relative contributions of localized and itinerant magnetism, perturb their balance, and thereby influence the spin dynamics. Therefore, the reduction of the magnon gap with increasing Fe content cannot presently be attributed simply to enhanced itinerancy [80]. Taken together, these studies indicate that Fe occupancy can influence several interconnected microscopic factors, including modifications to the electronic structure, SOC-mediated magnetic anisotropy, exchange interactions, site- and orbital-dependent electronic correlations, and potentially the balance between localized and itinerant magnetic contributions. However, how these different microscopic mechanisms evolve with Fe occupancy and contribute to the observed variation of the magnon gap near $n \simeq 3$ remains unresolved. Further systematic experimental investigations and composition-dependent theoretical studies are therefore required to shed light on the microscopic origin of this nontrivial composition dependence.

## IV. CONCLUSION

In summary, we have carried out a comprehensive ESR investigation of near-stoichiometric single-crystalline quasi-2D vdW ferromagnet $Fe_3GeTe_2$ across a wide range of frequencies, temperatures, and with the magnetic field applied along and perpendicular to the crystallographic $c$ direction, enabling us to disentangle and quantify the intrinsic magnetocrystalline anisotropy. Frequency-dependent ESR data establish $Fe_{3.03(3)}GeTe_2$ as an easy-axis ferromagnet with the easy axis aligned along the crystallographic $c$ direction. Temperature-dependent HF-ESR measurements reveal the evolution of magnetic anisotropy, with the internal field remaining almost constant up to 100 K ($\sim$ 3.2 T at 3 K). The intrinsic magnetocrystalline anisotropy shows an easy-axis character throughout the measured temperature range, reaching $\sim -5 \times 10^6$ erg cm$^{-3}$ at 3 K—comparatively larger than typical values reported for other vdW ferromagnets outside the $Fe_{3-x}GeTe_2$ family—confirming strong uniaxial anisotropy of $Fe_3GeTe_2$. The magnon excitation gap, $\Delta|_{3K} = 87.8 \pm 13.7$ GHz ($\approx$0.363 $\pm$ 0.057 meV) further underscores the large anisotropy in this system. Notably, our study concludes that even small variations in Fe content can lead to

substantial changes in the magnon gap at low temperatures, highlighting the sensitivity of spin dynamics to chemical composition in $Fe_3GeTe_2$. Furthermore, the shift of the ESR lines persists at temperatures even above $T_C$, suggesting the enhancement of ferromagnetic short-range spin correlations in $Fe_3GeTe_2$. These findings establish the $Fe_3GeTe_2$ as a model platform for exploring tunable spin-wave excitations and anisotropies in metallic vdW ferromagnets, and call for systematic composition-dependent experimental and theoretical investigations to unravel the microscopic origin of this nontrivial composition dependence.

## ACKNOWLEDGMENTS

The authors acknowledge R. Kluge and S. Wurmehl for the EDX measurements. R.P. acknowledges the Department of Science and Technology (DST), SNBNCBS, and IFW Dresden for funding. R.P. also acknowledges financial support from the Deutsche Forschungsgemeinschaft (DFG, German Research Foundation) through Project No. 589958266 (PA 5412/1-1) under the Walter Benjamin Programme. S.B. thanks CSIR, Government of India, for the Research Fellowship with Grant No. 09/080(1110)/2019-EMR-I. M.M. acknowledges funding from the DST, Government of India (CRG/2023/001100), and CSIR-Human Resource Development Group (HRDG) (03/1511/23/EMR-II). A.N.P. acknowledges funding from the DST Nano Mission with Grant No. DST/NM/TUE/QM-10/2019. This work was supported by the Deutsche Forschungsgemeinschaft (DFG) through Grant No. AL 1771/8-1 (Project No. 499461434), and within the Collaborative Research Center SFB 1143 "Correlated Magnetism–From Frustration to Topology" (Project-ID No. 247310070), and the Dresden-Würzburg Cluster of Excellence (EXC 2147) "ctd.qmat - Complexity, Topology and Dynamics in Quantum Matter" (Project-ID No. 390858490).

## DATA AVAILABILITY

The data that support the findings of this article are not publicly available. The data are available from the authors upon reasonable request.

## APPENDIX A: ENERGY-DISPERSIVE X-RAY SPECTROSCOPY (EDX) DATA

Energy-dispersive x-ray spectroscopy (EDX) measurements were carried out on the freshly cleaved bulk single-crystal sample of $Fe_3GeTe_2$. The corresponding EDX spectra, atomic percentages, and the scanning electron microscopy image are shown in Fig. 7. Measurements performed at multiple (more than ten) cleaved positions across the crystal indicate good compositional homogeneity with small error bars. The analysis reveals a slightly Fe-rich and near-stoichiometric composition, with average elemental contents of Fe = 3.03 ± 0.03, Ge = 0.89 ± 0.04, and Te = 2.00 ± 0.01, yielding an average composition of $Fe_{3.03(3)}Ge_{0.89(4)}Te_{2.00(1)}$ for our measured crystal. The Ge content varies between approximately 0.85 and 0.95 across different measured positions, suggesting a slight reduction in the Ge content.

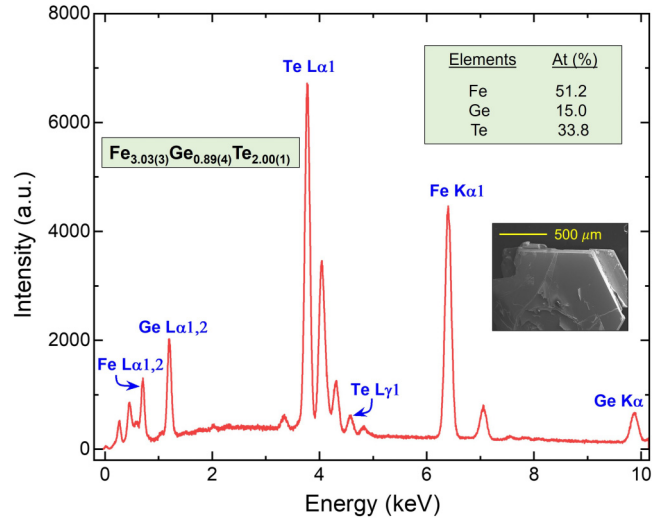



FIG. 7. Energy-dispersive x-ray spectroscopy (EDX) spectra of the measured bulk $Fe_3GeTe_2$ single crystal. Measurements were performed at multiple positions across the crystal, demonstrating good compositional homogeneity with small error bars. Inset: Atomic percentages of each element (top right) and a scanning electron microscopy image of the freshly cleaved crystal (bottom right). The averaged elemental composition indicates a slightly Fe-rich stoichiometry of $Fe_{3.03(3)}Ge_{0.89(4)}Te_{2.00(1)}$.

To further examine the reproducibility of the compositions, we performed additional EDX measurements on three separate crystals from the same growth batch, measuring three positions on each crystal (see Fig. 8). The corresponding average compositions of the individual crystals (see Table I) are $Fe_{3.02}Ge_{0.92}Te_{2.00}$, $Fe_{3.035}Ge_{0.917}Te_{2.00}$, and $Fe_{3.035}Ge_{0.917}Te_{2.00}$, yielding a batch-averaged composition of $Fe_{3.03(3)}Ge_{0.918(4)}Te_{2.00(0)}$. The relatively small variation within and between the crystals indicates that the reduced Ge content is reproducible across the growth batch rather than arising from local compositional inhomogeneity.

The small Ge deficiency may originate from the iodine-mediated chemical vapor transport growth process. In such a process, the deposited composition is set by the relative transport equilibria of the volatile iodide species rather than by the charge. Germanium is transported mainly through $GeI_2$ and $GeI_4$ species, which could be more volatile than the corresponding Fe and Te iodides under the present growth conditions. As a result, Ge may remain preferentially in the gas phase and at the source, and the crystals grown at the cold end could be Ge-poor relative to the nominal $Fe_3GeTe_2$ charge. Site substitution could contribute as well: The slight Fe excess together with the observed Ge deficiency may be consistent with partial occupation of the Ge site by Fe, accompanied by a small concentration of Ge vacancies [50,51,53,85]. However, EDX measurements alone cannot distinguish between Ge vacancies, partial site occupancy, and possible site substitution. Although similar Ge deficiencies have also been reported in some studies [50,86], there is currently no direct evidence that such small deviations in Ge content play a significant role in the magnetic properties discussed here. Rather, numerous previous studies have primarily identified nonstoichiometry on the Fe sublattice and

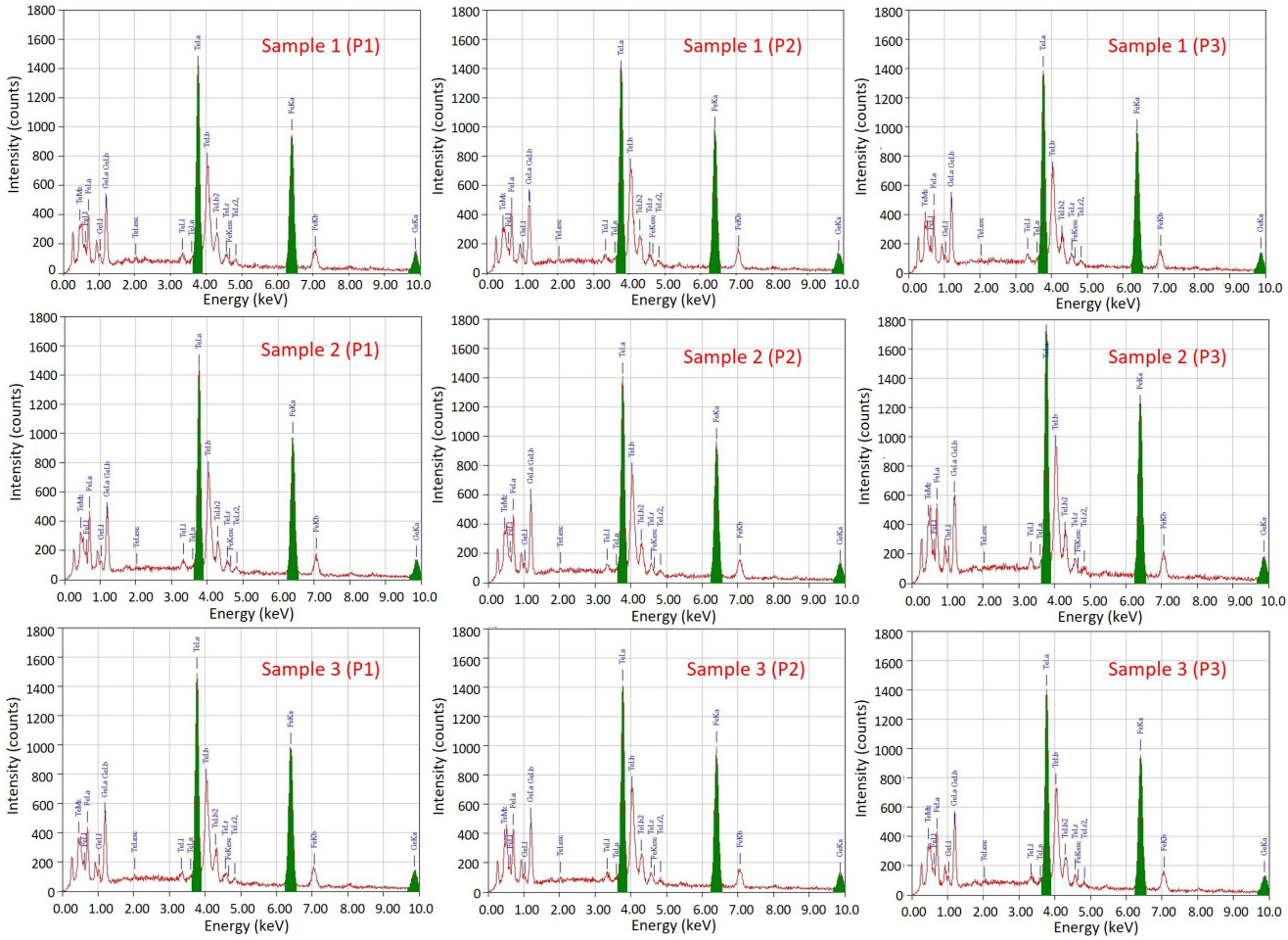



FIG. 8. EDX spectra on three different bulk $Fe_3GeTe_2$ crystals from the same growth batch with three different positions (P1, P2, P3) on each crystal.

have established that the variations in Fe occupancy or Fe-site vacancies strongly influence the magnetic and electronic properties of $Fe_{3-x}GeTe_2$ [49–53,85]. In this context, the term "near-stoichiometric" is used to emphasize that the Fe content is very close to the ideal $n = 3$ limit, which is the primary compositional variable and one of the main focuses of the present work on the influence of Fe stoichiometry on the magnetic anisotropy and spin dynamics of $Fe_3GeTe_2$.

TABLE I. Elemental composition details of three $Fe_3GeTe_2$ crystals from the same growth batch. Measurements were performed at three different positions (P1–P3) on each crystal.

| | | Atomic percentage (at. %) | | | Normalized composition | | |
|---|---|---|---|---|---|---|---|
| Sample | Position | Fe | Ge | Te | Fe | Ge | Te |
| **Sample 1** | P1 | 51.0 | 15.3 | 33.7 | 3.04 | 0.91 | 2.01 |
| | P2 | 50.8 | 15.7 | 33.5 | 3.02 | 0.93 | 1.99 |
| | P3 | 50.6 | 15.5 | 33.6 | 3.01 | 0.92 | 2.00 |
| | **Mean** | **50.8** | **15.5** | **33.6** | **3.02** | **0.92** | **2.00** |
| **Sample 2** | P1 | 50.8 | 15.6 | 33.6 | 3.02 | 0.93 | 2.00 |
| | P2 | 51.0 | 15.3 | 33.7 | 3.04 | 0.91 | 2.01 |
| | P3 | 51.0 | 15.5 | 33.5 | 3.03 | 0.92 | 1.99 |
| | **Mean** | **50.933** | **15.467** | **33.6** | **3.035** | **0.917** | **2.00** |
| **Sample 3** | P1 | 50.8 | 15.6 | 33.6 | 3.02 | 0.93 | 2.00 |
| | P2 | 51.1 | 15.3 | 33.6 | 3.04 | 0.91 | 2.00 |
| | P3 | 50.9 | 15.5 | 33.6 | 3.03 | 0.92 | 2.00 |
| | **Mean** | **50.933** | **15.467** | **33.60** | **3.035** | **0.917** | **2.00** |
| **Average of all three samples** | | **50.89** | **15.478** | **33.6** | **3.03** | **0.918** | **2.00** |

## APPENDIX B: FREQUENCY DEPENDENCE OF THE RESONANCE FIELDS AT 300 K

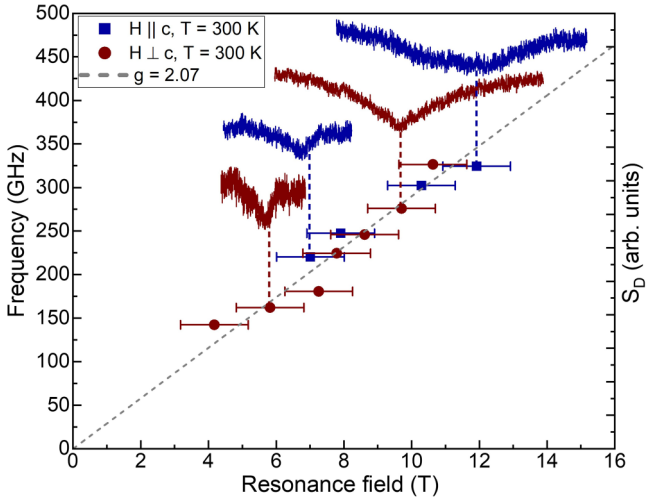



FIG. 9. Frequency dependence of the resonance fields $H_{res}$ at $T = 300$ K measured in $\mathbf{H} \parallel \mathbf{c}$ (blue squares) and in $\mathbf{H} \perp \mathbf{c}$ (red circles) configurations. Dashed lines represent the paramagnetic response estimated with Eq. (1) (main text) with the average $g$ factors given in the legends. Representative normalized and vertically shifted spectra are shown for some of the frequencies (right vertical axis) with respective colors following respective magnetic field orientations.

## APPENDIX C: IN-PLANE ANISOTROPY FROM HF-ESR MEASUREMENTS

To examine the anisotropy within the *ab* plane, the $Fe_3GeTe_2$ crystal was rotated by 90° from its initial in-plane orientation (IP1). In this alternative in-plane setup (IP2), the frequency dependence of the resonance fields ($\nu$ vs $H$) was recorded at temperatures of 3 and 100 K. A comparison between the results from configurations IP1 and IP2 is presented in Fig. 10. The data demonstrate that, within the margin of error, both orientations produce comparable outcomes at both temperatures, indicating the absence of any measurable in-plane anisotropy in this $Fe_3GeTe_2$ sample, which is consistent with earlier findings from magnetization studies [40].

## APPENDIX D: TEMPERATURE DEPENDENCE OF THE RESONANCE FIELD

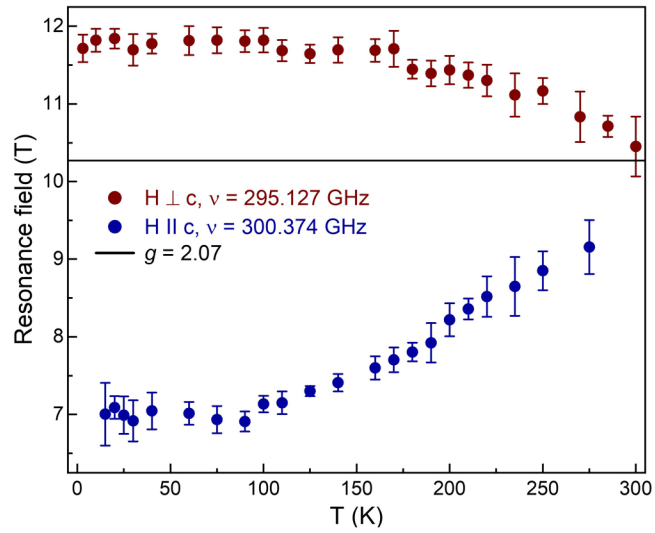



FIG. 11. Temperature dependence of the resonance field, $H_{res}$, at a microwave frequency $\nu$ of ≈300 GHz with an external magnetic field applied parallel (blue circles) and perpendicular (red circles) to the $c$ axis. The black horizontal line indicates the expected paramagnetic line with the $g$ factor, $g = 2.07$.

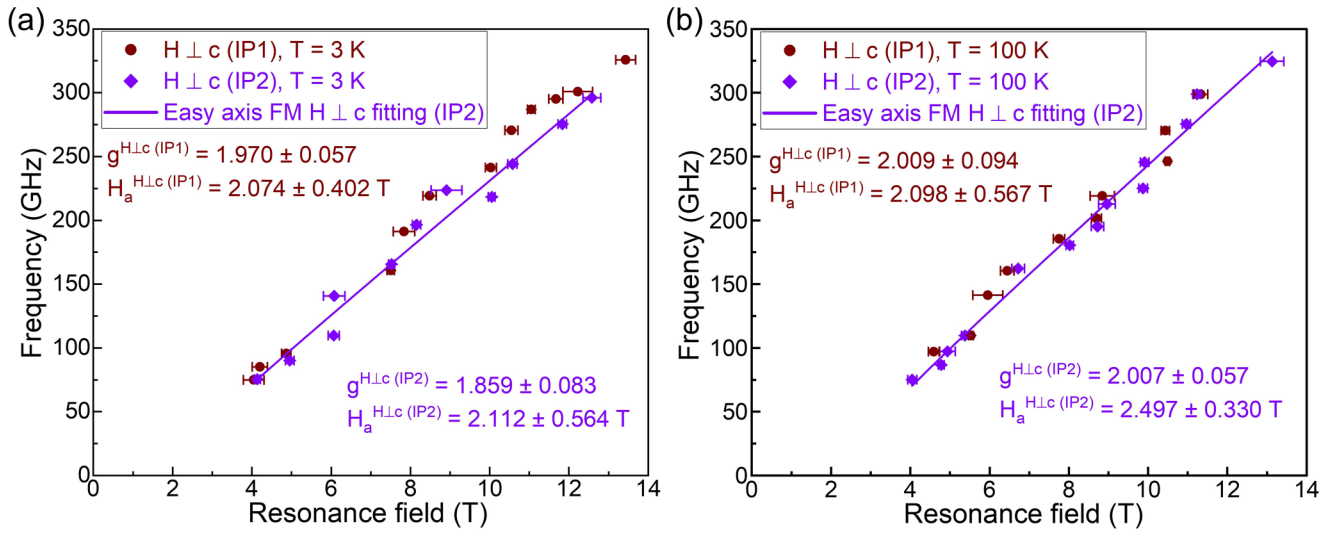



FIG. 10. Frequency dependence of the resonance fields $H_{res}$ measured at (a) 3 K and (b) 100 K along two mutually orthogonal in-plane directions, labeled IP1 ($\mathbf{H} \perp \mathbf{c}$) and IP2 (newly measured, perpendicular to the IP1 in-plane). The violet line represents the fit to the IP2 data. The fitting parameters are displayed in the respective insets.

## APPENDIX E: MAGNETIC FIELD DEPENDENCE OF THE MAGNETIZATION

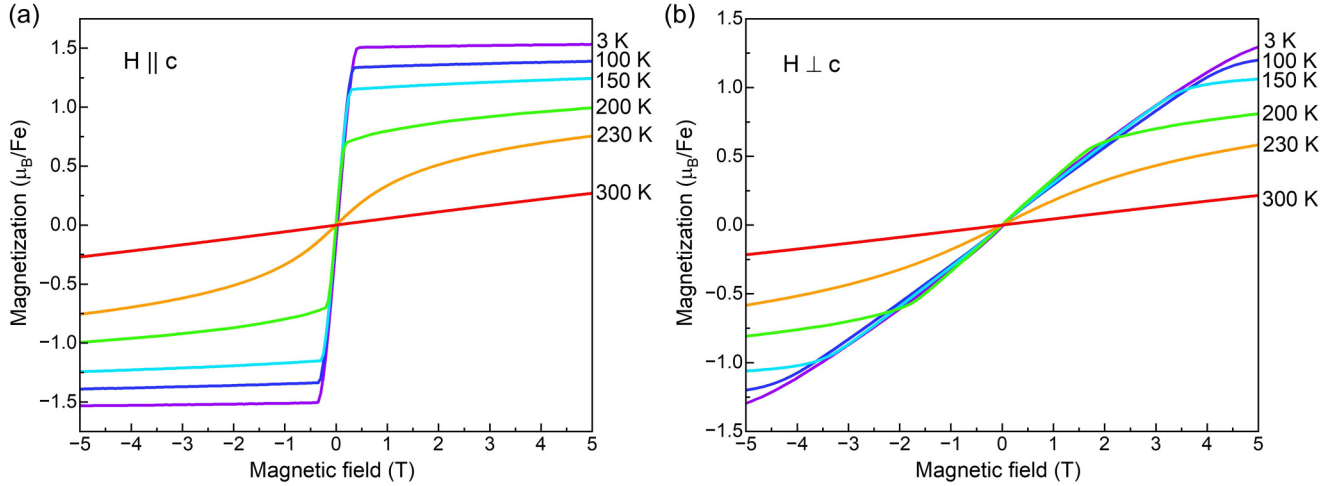



FIG. 12. Magnetic field dependence of the magnetization measured for (a) **H** ∥ **c** and (b) **H** ⊥ **c** configurations at different temperatures, showing that the magnetic easy axis is the *c* axis of the $Fe_3GeTe_2$ crystal.

## APPENDIX F: MAGNETIC-FIELD-INDUCED INCREASE OF THE ORDERING TEMPERATURE

To investigate the magnetic-field dependence of the Curie temperature, $T_C$, we performed temperature-dependent magnetization ($M$-$T$) measurements under various external magnetic fields ($H$) applied along the magnetic easy axis ($c$ axis) of the $Fe_3GeTe_2$ crystal (see Fig. 13). The $T_C$ is determined from the minimum in the temperature derivative of the magnetization, $dM/dT$, as shown in Fig. 13(b) and Fig. 1(b) [28,49]. Here, for magnetic fields above 0.5 T, $T_C$ increases monotonically with increasing $H$ and reaches ∼245 K at 7 T, as shown in Fig. 13(b) (inset). This field-induced enhancement of $T_C$ is expected for ferromagnets, as an external magnetic field favors parallel spin alignment, thereby stabilizing the ordered state against thermal fluctuations [49].

## APPENDIX G: CALCULATION OF TOTAL MAGNETIC ANISOTROPY ENERGY (MAE) FROM STATIC MAGNETIZATION DATA

To qualitatively determine the temperature dependence of the total anisotropy field, another method, known as the *area method*, was employed [7,72,87,88]. This method provides a reasonable estimate of $H_a$ for single-sublattice, uniaxial ferromagnets [72,87]. For this, magnetization isotherms $M(H)$ were recorded at various temperatures for both **H** ∥ **c** and **H** ⊥ **c** orientations (see Fig. 12). From these static measurements,

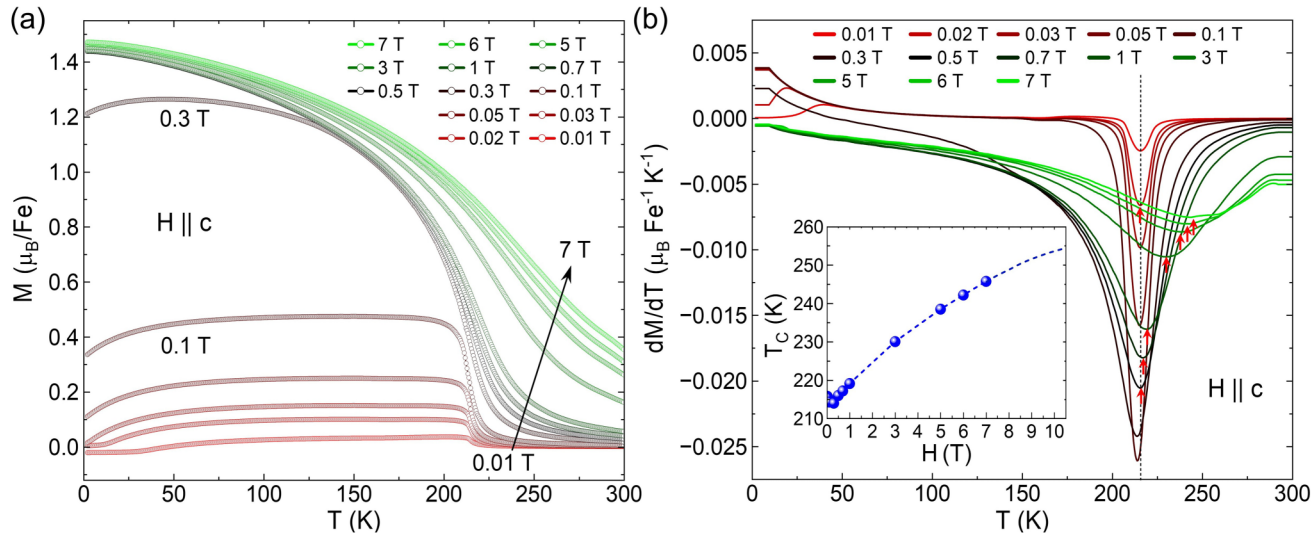



FIG. 13. (a) Temperature-dependent magnetization ($M$-$T$) measurements under various external magnetic fields ($H$) applied along the $c$ axis of $Fe_3GeTe_2$. (b) Temperature dependence of the temperature derivative of magnetization, $dM/dT$. The minimum in $dM/dT$ gives the $T_C$ of the crystal, indicated by the red arrow. Inset: External magnetic field dependence of $T_C$. The dashed line is the guide for the eyes.

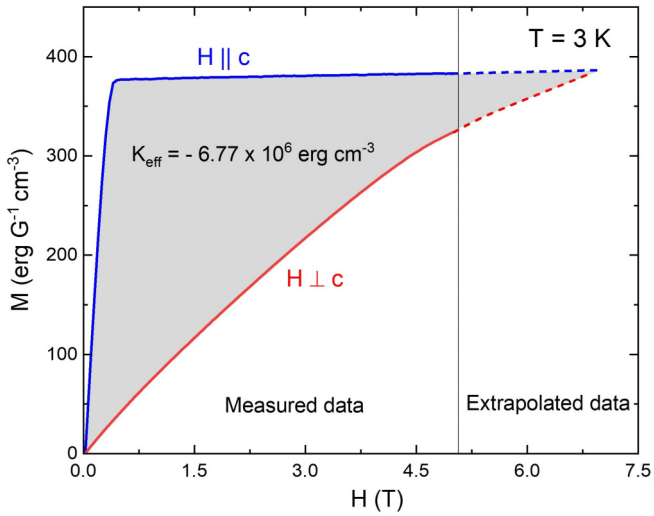



FIG. 14. Magnetization isotherms $M(H)$ measured at 3 K for $\mathbf{H} \parallel \mathbf{c}$ and $\mathbf{H} \perp \mathbf{c}$ orientations. The gray shaded area indicates the area difference between the two curves, which is a qualitative measure of effective magnetic anisotropy energy (MAE) at 3 K.

the effective magnetic anisotropy energy (MAE) ($K_{\text{eff}}$) was qualitatively estimated by integrating the magnetization-field ($M$-$H$) curves following Refs. [7,72,87–90]:

$$K_{\text{eff}} = \mu_0 \int_0^{M_s} [H_c(M) - H_{ab}(M)]\, dM, \qquad \text{(G1)}$$

where $M_s$ is the saturation magnetization, and $H_{ab}$ and $H_c$ denote the in-plane ($\mathbf{H} \perp \mathbf{c}$) and out-of-plane ($\mathbf{H} \parallel \mathbf{c}$) magnetic fields, respectively. The magnetic energy required to change the sample's magnetization by an infinitesimal amount $dM$ under an external magnetic field $H$ can be represented by $\mu_0 H\, dM$ [72,87]. Consequently, the integral in Eq. (G1) represents the area difference between the two magnetization curves and provides a qualitative measure of the effective MAE (see Fig. 14), which includes contributions from both magnetocrystalline and shape anisotropies for easy-axis ferromagnets [87]. The temperature-dependent values of $K_{\text{eff}}$ obtained from this analysis are presented and compared with those obtained from HF-ESR data, as plotted in Fig. 15. The corresponding total anisotropy field, calculated using $H_a^{\text{mag}} = 2K_{\text{eff}}/M_s$, is plotted in Fig. 4(a) (main text) and exhibits good agreement with those derived from the HF-ESR measurements.

## APPENDIX H: TEMPERATURE DEPENDENCE OF TOTAL MAGNETIC ANISOTROPY ENERGY (MAE)

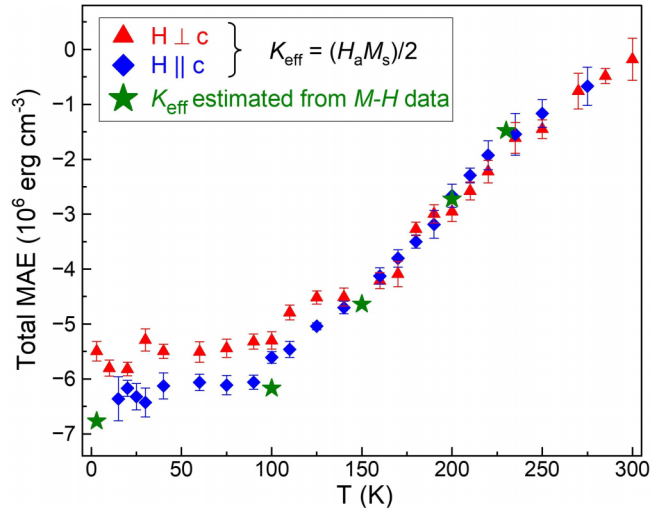



FIG. 15. Temperature dependence of total MAE ($K_{\text{eff}}$) is estimated from the HF-ESR data, with an external magnetic field applied parallel (blue diamonds) and perpendicular (red triangles) to the $c$ axis. The total MAE ($K_{\text{eff}}$), estimated from the $M - H$ data followed by Eq. (3) (main text), is plotted with green stars, well matching the results obtained from HF-ESR.

## APPENDIX I: TEMPERATURE DEPENDENCE OF THE SATURATION MAGNETIZATION

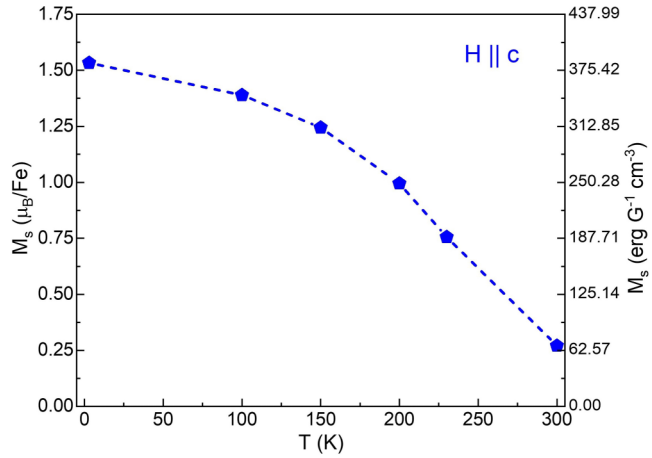



FIG. 16. Temperature dependence of the saturation magnetization $M_s$ for $\mathbf{H} \parallel \mathbf{c}$ configuration.

## APPENDIX J: TEMPERATURE DEPENDENCE OF THE DEMAGNETIZATION FIELD AND ESTIMATED INTRINSIC MAGNETIC ANISOTROPY FIELD

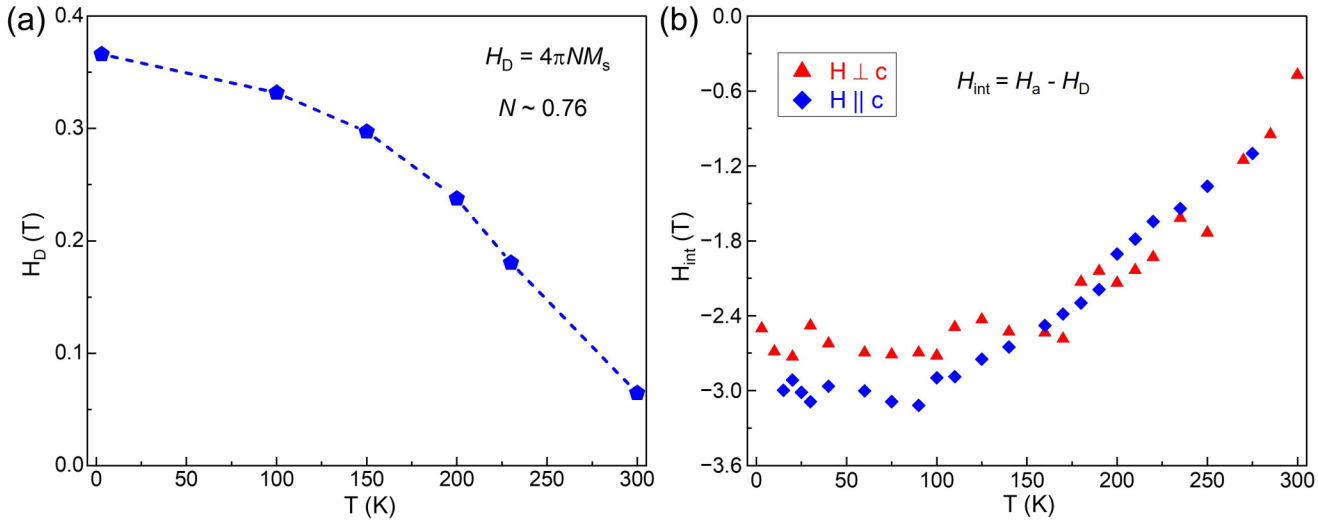



FIG. 17. (a) Temperature dependence of the demagnetization field $H_D$, estimated from the temperature-dependent saturation magnetization data and the calculated demagnetization factor. (b) Temperature dependence of the intrinsic magnetic anisotropy field ($H_{int}$), estimated from the total magnetic anisotropy field and demagnetization field, in the $\mathbf{H} \perp \mathbf{c}$ and $\mathbf{H} \parallel \mathbf{c}$ configurations, respectively.


[1] K. S. Novoselov, A. Mishchenko, A. Carvalho, and A. H. Castro Neto, 2D materials and van der Waals heterostructures, Science **353**, aac9439 (2016).

[2] E. C. Ahn, 2D materials for spintronic devices, npj 2D Mater. Appl. **4**, 17 (2020).

[3] C. Gong and X. Zhang, Two-dimensional magnetic crystals and emergent heterostructure devices, Science **363**, eaav4450 (2019).

[4] Q. Hao, H. Dai, M. Cai, X. Chen, Y. Xing, H. Chen, T. Zhai, X. Wang, and J. Han, 2D magnetic heterostructures and emergent spintronic devices, Adv. Electron. Mater. **8**, 2200164 (2022).

[5] K. S. Burch, D. Mandrus, and J.-G. Park, Magnetism in two-dimensional van der Waals materials, Nature (London) **563**, 47 (2018).

[6] N. D. Mermin and H. Wagner, Absence of ferromagnetism or antiferromagnetism in one- or two-dimensional isotropic Heisenberg models, Phys. Rev. Lett. **17**, 1133 (1966).

[7] A. H. Morrish, *The Physical Principles of Magnetism* (Wiley-IEEE Press, New York, 2001).

[8] J. M. D. Coey, *Magnetism and Magnetic Materials* (Cambridge University Press, Cambridge, 2010).

[9] V. Kataev, B. Büchner, and A. Alfonsov, Electron spin resonance spectroscopy on magnetic van der Waals compounds, Appl. Magn. Reson. **55**, 923 (2024).

[10] C. W. Cho, A. Pawbake, N. Aubergier, A. L. Barra, K. Mosina, Z. Sofer, M. E. Zhitomirsky, C. Faugeras, and B. A. Piot, Microscopic parameters of the van der Waals CrSBr antiferromagnet from microwave absorption experiments, Phys. Rev. B **107**, 094403 (2023).

[11] R. Pal, J. J. Abraham, A. Mistonov, S. Mishra, N. Stilkerich, S. Mondal, P. Mandal, A. N. Pal, J. Geck, B. Büchner, V. Kataev, and A. Alfonsov, Disentangling the unusual magnetic anisotropy of the near-room-temperature ferromagnet $Fe_4GeTe_2$, Adv. Funct. Mater. **34**, 2402551 (2024).

[12] F. Moro, S. Ke, A. G. del Águila, A. Söll, Z. Sofer, Q. Wu, M. Yue, L. Li, X. Liu, and M. Fanciulli, Revealing 2D magnetism in a bulk CrSBr single crystal by electron spin resonance, Adv. Funct. Mater. **32**, 2207044 (2022).

[13] I. Lee, F. G. Utermohlen, D. Weber, K. Hwang, C. Zhang, J. van Tol, J. E. Goldberger, N. Trivedi, and P. Chris Hammel, Fundamental spin interactions underlying the magnetic anisotropy in the Kitaev ferromagnet $CrI_3$, Phys. Rev. Lett. **124**, 017201 (2020).

[14] R. Pal, K. Deb, N. Kumar, B. Büchner, A. Alfonsov, and V. Kataev, Ferromagnetic resonance spectroscopy on the kagome magnet $MgMn_6Sn_6$, Appl. Magn. Reson. **56**, 1507 (2025).

[15] X. Wang, Z. Shang, C. Zhang, J. Kang, T. Liu, X. Wang, S. Chen, H. Liu, W. Tang, Y.-J. Zeng, J. Guo, Z. Cheng, L. Liu, D. Pan, S. Tong, B. Wu, Y. Xie, G. Wang, J. Deng, T. Zhai, *et al.*, Electrical and magnetic anisotropies in van der Waals multiferroic $CuCrP_2S_6$, Nat. Commun. **14**, 840 (2023).

[16] B. G. Beier, E. S. Beier, J. Arneth, E. Brücher, R. K. Kremer, and R. Klingeler, Elucidating the origin of long-range ferromagnetic order in $Fe_3GeTe_2$ by low-energy magnon excitation studies, Phys. Rev. B **112**, 214414 (2025).

[17] A. Alfonsov, K. Mehlawat, A. Zeugner, A. Isaeva, B. Büchner, and V. Kataev, Magnetic-field tuning of the spin dynamics in the magnetic topological insulators $(MnBi_2Te_4)(Bi_2Te_3)_n$, Phys. Rev. B **104**, 195139 (2021).

[18] L. Alahmed, B. Nepal, J. Macy, W. Zheng, B. Casas, A. Sapkota, N. Jones, A. R. Mazza, M. Brahlek, W. Jin, M. Mahjouri-Samani, S. S.-L. Zhang, C. Mewes, L. Balicas, T. Mewes, and P. Li, Magnetism and spin dynamics in

room-temperature van der Waals magnet $Fe_5GeTe_2$, 2D Mater. **8**, 045030 (2021).

[19] J. Zeisner, K. Mehlawat, A. Alfonsov, M. Roslova, T. Doert, A. Isaeva, B. Büchner, and V. Kataev, Electron spin resonance and ferromagnetic resonance spectroscopy in the high-field phase of the van der Waals magnet $CrCl_3$, Phys. Rev. Mater. **4**, 064406 (2020).

[20] B. Huang, G. Clark, E. Navarro-Moratalla, D. R. Klein, R. Cheng, K. L. Seyler, D. Zhong, E. Schmidgall, M. A. McGuire, D. H. Cobden, W. Yao, D. Xiao, P. Jarillo-Herrero, and X. Xu, Layer-dependent ferromagnetism in a van der Waals crystal down to the monolayer limit, Nature (London) **546**, 270 (2017).

[21] C. Gong, L. Li, Z. Li, H. Ji, A. Stern, Y. Xia, T. Cao, W. Bao, C. Wang, Y. Wang, Z. Q. Qiu, R. J. Cava, S. G. Louie, J. Xia, and X. Zhang, Discovery of intrinsic ferromagnetism in two-dimensional van der Waals crystals, Nature (London) **546**, 265 (2017).

[22] X. Jiang, Q. Liu, J. Xing, N. Liu, Y. Guo, Z. Liu, and J. Zhao, Recent progress on 2D magnets: Fundamental mechanism, structural design and modification, Appl. Phys. Rev. **8**, 031305 (2021).

[23] X. Shen, H. Chen, Y. Li, H. Xia, F. Zeng, J. Xu, H. Y. Kwon, Y. Ji, C. Won, W. Zhang, and Y. Wu, Multi-domain ferromagnetic resonance in magnetic van der Waals crystals $CrI_3$ and $CrBr_3$, J. Magn. Magn. Mater. **528**, 167772 (2021).

[24] T. J. Williams, A. A. Aczel, M. D. Lumsden, S. E. Nagler, M. B. Stone, J. Q. Yan, and D. Mandrus, Magnetic correlations in the quasi-two-dimensional semiconducting ferromagnet $CrSiTe_3$, Phys. Rev. B **92**, 144404 (2015).

[25] J. U. Lee, S. Lee, J. H. Ryoo, S. Kang, T. Y. Kim, P. Kim, C. H. Park, J. G. Park, and H. Cheong, Ising-type magnetic ordering in atomically thin $FePS_3$, Nano Lett. **16**, 7433 (2016).

[26] X. Wang, J. Cao, H. Li, Z. Lu, A. Cohen, A. Haldar, H. Kitadai, Q. Tan, K. S. Burch, D. Smirnov, W. Xu, S. Sharifzadeh, L. Liang, and X. Ling, Electronic Raman scattering in the 2D antiferromagnet $NiPS_3$, Sci. Adv. **8**, eabl7707 (2022).

[27] Y. Deng, Y. Yu, Y. Song, J. Zhang, N. Z. Wang, Z. Sun, Y. Yi, Y. Z. Wu, S. Wu, J. Zhu, J. Wang, X. H. Chen, and Y. Zhang, Gate-tunable room-temperature ferromagnetism in two-dimensional $Fe_3GeTe_2$, Nature (London) **563**, 94 (2018).

[28] R. Pal, B. Pal, S. Mondal, R. O. Sharma, T. Das, P. Mandal, and A. N. Pal, Spin-reorientation driven emergent phases and unconventional magnetotransport in quasi-2D vdW ferromagnet $Fe_4GeTe_2$, npj 2D Mater. Appl. **8**, 30 (2024).

[29] J. Seo, D. Y. Kim, E. S. An, K. Kim, G.-Y. Kim, S.-Y. Hwang, D. W. Kim, B. G. Jang, H. Kim, G. Eom, S. Y. Seo, R. Stania, M. Muntwiler, J. Lee, K. Watanabe, T. Taniguchi, Y. J. Jo, J. Lee, B. I. Min, M. H. Jo, *et al.*, Nearly room temperature ferromagnetism in a magnetic metal-rich van der Waals metal, Sci. Adv. **6**, eaay8912 (2020).

[30] S. Bera, S. K. Pradhan, M. S. Khan, R. Pal, B. Pal, S. Kalimuddin, A. Bera, B. Das, A. N. Pal, and M. Mondal, Unravelling the nature of spin reorientation transition in quasi-2D vdW magnetic material, $Fe_4GeTe_2$, J. Magn. Magn. Mater. **565**, 170257 (2023).

[31] C. Tan, W.-Q. Xie, G. Zheng, N. Aloufi, S. Albarakati, M. Algarni, J. Li, J. Partridge, D. Culcer, X. Wang, J. B. Yi, M. Tian, Y. Xiong, Y.-J. Zhao, and L. Wang, Gate-controlled magnetic phase transition in a van der Waals magnet $Fe_5GeTe_2$, Nano Lett. **21**, 5599 (2021).

[32] R. Pal, M. N. Hasan, D. Das, C. Nayak, M. Deka, N. Salehi, M. Pereiro, S. Mondal, A. Misra, A. Singha, P. Mandal, D. Karmakar, and A. N. Pal, Spin reorientation driven renormalization of spin–phonon coupling in $Fe_4GeTe_2$, ACS Nano **20**, 24621 (2026).

[33] A. F. May, C. A. Bridges, and M. A. McGuire, Physical properties and thermal stability of $Fe_{5-x}GeTe_2$ single crystals, Phys. Rev. Mater. **3**, 104401 (2019).

[34] Z. Fei, B. Huang, P. Malinowski, W. Wang, T. Song, J. Sanchez, W. Yao, D. Xiao, X. Zhu, A. F. May, W. Wu, D. H. Cobden, J.-H. Chu, and X. Xu, Two-dimensional itinerant ferromagnetism in atomically thin $Fe_3GeTe_2$, Nat. Mater. **17**, 778 (2018).

[35] R. Pal, S. Bera, B. Pal, M. Mondal, and A. N. Pal, Intrinsic room temperature ferromagnetism in van der Waals $Fe_5GeTe_2$ crystal, AIP Conf. Proc. **3067**, 20002 (2024).

[36] L. Ni, Z. Chen, W. Li, X. Lu, Y. Yan, L. Zhang, C. Yan, Y. Chen, Y. Gu, Y. Li, R. Zhang, Y. Zhai, R. Liu, Y. Yang, and Y. Xu, Magnetic dynamics of two-dimensional itinerant ferromagnet $Fe_3GeTe_2$, Chin. Phys. B **30**, 097501 (2021).

[37] S. Albarakati, C. Tan, Z. J. Chen, J. G. Partridge, G. Zheng, L. Farrar, E. L. Mayes, M. R. Field, C. Lee, Y. Wang, Y. Xiong, M. Tian, F. Xiang, A. R. Hamilton, O. A. Tretiakov, D. Culcer, Y. J. Zhao, and L. Wang, Antisymmetric magnetoresistance in van der Waals $Fe_3GeTe_2$/graphite/$Fe_3GeTe_2$ trilayer heterostructures, Sci. Adv. **5**, eaaw0409 (2019).

[38] L. Zhou, J. Huang, M. Tang, C. Qiu, F. Qin, C. Zhang, Z. Li, D. Wu, and H. Yuan, Gate-tunable spin valve effect in $Fe_3GeTe_2$-based van der Waals heterostructures, InfoMat. **5**, e12371 (2022).

[39] B. Chen, J. Yang, H. Wang, M. Imai, H. Ohta, C. Michioka, K. Yoshimura, and M. Fang, Magnetic properties of layered itinerant electron ferromagnet $Fe_3GeTe_2$, J. Phys. Soc. Jpn. **82**, 124711 (2013).

[40] Y. Wang, C. Xian, J. Wang, B. Liu, L. Ling, L. Zhang, L. Cao, Z. Qu, and Y. Xiong, Anisotropic anomalous Hall effect in triangular itinerant ferromagnet $Fe_3GeTe_2$, Phys. Rev. B **96**, 134428 (2017).

[41] Y. Zhang, H. Lu, X. Zhu, S. Tan, W. Feng, Q. Liu, W. Zhang, Q. Chen, Y. Liu, X. Luo, D. Xie, L. Luo, Z. Zhang, and X. Lai, Emergence of Kondo lattice behavior in a van der Waals itinerant ferromagnet, $Fe_3GeTe_2$, Sci. Adv. **4**, eaao6791 (2018).

[42] Y. Xu, Y.-C. Wang, X. Jin, H. Liu, Y. Liu, H. Song, and F. Tian, Mechanism of magnetic phase transition in correlated magnetic metal: Insight into itinerant ferromagnet $Fe_{3-\delta}GeTe_2$, Commun. Phys. **7**, 381 (2024).

[43] T. J. Kim, S. Ryee, and M. J. Han, $Fe_3GeTe_2$: A site-differentiated Hund metal, npj Comput. Mater. **8**, 245 (2022).

[44] K. Kim, J. Seo, E. Lee, K. T. Ko, B. S. Kim, B. G. Jang, J. M. Ok, J. Lee, Y. J. Jo, W. Kang, J. H. Shim, C. Kim, H. W. Yeom, B. Il Min, B. J. Yang, and J. S. Kim, Large anomalous Hall current induced by topological nodal lines in a ferromagnetic van der Waals semimetal, Nat. Mater. **17**, 794 (2018).

[45] B. Ding, Z. Li, G. Xu, H. Li, Z. Hou, E. Liu, X. Xi, F. Xu, Y. Yao, and W. Wang, Observation of magnetic skyrmion bubbles in a van der Waals ferromagnet $Fe_3GeTe_2$, Nano Lett. **20**, 868 (2020).

[46] C. Tan, J. Lee, S. G. Jung, T. Park, S. Albarakati, J. Partridge, M. R. Field, D. G. McCulloch, L. Wang, and C. Lee, Hard magnetic properties in nanoflake van der Waals $Fe_3GeTe_2$, Nat. Commun. **9**, 1554 (2018).

[47] X. Hu, Y. Zhao, X. Shen, A. V. Krasheninnikov, Z. Chen, and L. Sun, Enhanced ferromagnetism and tunable magnetism in $Fe_3GeTe_2$ monolayer by strain engineering, ACS Applied Materials & Interfaces **12**, 26367 (2020).

[48] H. Weerahennedige, M. Irziqat, D. Vithanage, H. Weerarathne, Z. Ronau, G. Sumanasekera, and J. B. Jasinski, The effects of thickness, polarization, and strain on vibrational modes of 2D $Fe_3GeTe_2$, Surf. Interfaces **51**, 104797 (2024).

[49] Y. Liu, V. N. Ivanovski, and C. Petrovic, Critical behavior of the van der Waals bonded ferromagnet $Fe_{3-x}GeTe_2$, Phys. Rev. B **96**, 144429 (2017).

[50] A. F. May, S. Calder, C. Cantoni, H. Cao, and M. A. McGuire, Magnetic structure and phase stability of the van der Waals bonded ferromagnet $Fe_{3-x}GeTe_2$, Phys. Rev. B **93**, 014411 (2016).

[51] D. A. Mayoh, G. D. A. Wood, S. J. R. Holt, G. Beckett, E. J. L. Dekker, M. R. Lees, and G. Balakrishnan, Effects of Fe deficiency and Co substitution in polycrystalline and single crystals of $Fe_3GeTe_2$, Crystal Growth & Design **21**, 6786 (2021).

[52] D. Backes, R. Fujita, L. S. I. Veiga, D. A. Mayoh, G. D. A. Wood, S. S. Dhesi, G. Balakrishnan, G. van der Laan, and T. Hesjedal, Valence-state mixing and reduced magnetic moment in $Fe_{3-\delta}GeTe_2$ single crystals with varying Fe content probed by x-ray spectroscopy, Nanotechnology **35**, 395709 (2024).

[53] S. Bera, S. K. Pradhan, R. Pal, B. Pal, A. Bera, S. Kalimuddin, M. Das, D. S. Roy, H. Afzal, A. N. Pal, and M. Mondal, Enhanced coercivity and emergent spin-cluster-glass state in 2D ferromagnetic material, $Fe_3GeTe_2$, J. Magn. Magn. Mater. **583**, 171052 (2023).

[54] J. Yi, H. Zhuang, Q. Zou, Z. Wu, G. Cao, S. Tang, S. A. Calder, P. R. Kent, D. Mandrus, and Z. Gai, Competing antiferromagnetism in a quasi-2D itinerant ferromagnet: $Fe_3GeTe_2$, 2D Mater. **4**, 011005 (2017).

[55] M. Farle, Ferromagnetic resonance of ultrathin metallic layers, Rep. Prog. Phys. **61**, 755 (1998).

[56] S. S. Kalarickal, P. Krivosik, M. Wu, C. E. Patton, M. L. Schneider, P. Kabos, T. J. Silva, and J. P. Nibarger, Ferromagnetic resonance linewidth in metallic thin films: Comparison of measurement methods, J. Appl. Phys. **99**, 093909 (2006).

[57] P. Pirro, T. Brächer, A. V. Chumak, B. Lägel, C. Dubs, O. Surzhenko, P. Görnert, B. Leven, and B. Hillebrands, Spin-wave excitation and propagation in microstructured waveguides of yttrium iron garnet/Pt bilayers, Appl. Phys. Lett. **104**, 012402 (2014).

[58] A. Abragam and B. Bleaney, *Electron Paramagnetic Resonance of Transition Ions* (Oxford University Press, Oxford, 2012).

[59] E. A. Turov, in *Physical Properties of Magnetically Ordered Crystals*, edited by A. Tybulewicz and S. Chomet (Academic Press, New York, 1965).

[60] T. Holstein and H. Primakoff, Field dependence of the intrinsic domain magnetization of a ferromagnet, Phys. Rev. **58**, 1098 (1940).

[61] Y. Yang, F. Meng, W. Liu, J. Li, J. Zhang, J. Fan, C. Ma, M. Ge, L. Pi, Z. Qu, and L. Zhang, Electron spin resonance study of the van der Waals ferromagnet $Fe_5GeTe_2$, J. Magn. Magn. Mater. **629**, 173251 (2025).

[62] M. Jonak, E. Walendy, J. Arneth, M. Abdel-Hafiez, and R. Klingeler, Low-energy magnon excitations and emerging anisotropic nature of short-range order in $CrI_3$, Phys. Rev. B **106**, 214412 (2022).

[63] J. Dillon Jr. and C. Olson, Magnetization, resonance, and optical properties of the ferromagnet $CrI_3$, J. Appl. Phys. **36**, 1259 (1965).

[64] Z. Li, D.-H. Xu, X. Li, H.-J. Liao, X. Xi, Y.-C. Yu, and W. Wang, Anomalous spin dynamics in a two-dimensional magnet induced by anisotropic critical fluctuations, Phys. Rev. B **106**, 054427 (2022).

[65] S. Khan, C. W. Zollitsch, D. M. Arroo, H. Cheng, I. Verzhbitskiy, A. Sud, Y. P. Feng, G. Eda, and H. Kurebayashi, Spin dynamics study in layered van der Waals single-crystal $Cr_2Ge_2Te_6$, Phys. Rev. B **100**, 134437 (2019).

[66] J. Zeisner, A. Alfonsov, S. Selter, S. Aswartham, M. P. Ghimire, M. Richter, J. van den Brink, B. Büchner, and V. Kataev, Magnetic anisotropy and spin-polarized two-dimensional electron gas in the van der Waals ferromagnet $Cr_2Ge_2Te_6$, Phys. Rev. B **99**, 165109 (2019).

[67] Y. Wang, Q. Fu, S. Ji, X. Yin, Y. Chen, R. Liu, and X. Li, Temperature-dependent magnetic order of two-dimensional ferromagnetic $Cr_2Ge_2Te_6$ single crystal, J. Alloys Compd. **931**, 167401 (2023).

[68] S. Calder, A. I. Kolesnikov, and A. F. May, Magnetic excitations in the quasi-two-dimensional ferromagnet $Fe_{3-x}GeTe_2$ measured with inelastic neutron scattering, Phys. Rev. B **99**, 094423 (2019).

[69] S. Bao, W. Wang, Y. Shangguan, Z. Cai, Z.-Y. Dong, Z. Huang, W. Si, Z. Ma, R. Kajimoto, K. Ikeuchi, S.-i. Yano, S.-L. Yu, X. Wan, J.-X. Li, and J. Wen, Neutron spectroscopy evidence on the dual nature of magnetic excitations in a van der Waals metallic ferromagnet $Fe_{2.72}GeTe_2$, Phys. Rev. X **12**, 011022 (2022).

[70] J. A. Osborn, Demagnetizing factors of the general ellipsoid, Phys. Rev. **67**, 351 (1945).

[71] D. C. Cronemeyer, Demagnetization factors for general ellipsoids, J. Appl. Phys. **70**, 2911 (1991).

[72] B. D. Cullity and C. D. Graham, *Introduction to Magnetic Materials*, 2nd ed. (John Wiley & Sons, USA, 2011).

[73] J.-X. Zhu, M. Janoschek, D. S. Chaves, J. C. Cezar, T. Durakiewicz, F. Ronning, Y. Sassa, M. Mansson, B. L. Scott, N. Wakeham, E. D. Bauer, and J. D. Thompson, Electronic correlation and magnetism in the ferromagnetic metal $Fe_3GeTe_2$, Phys. Rev. B **93**, 144404 (2016).

[74] Q. Liu, J. Xing, Z. Jiang, Y. Guo, X. Jiang, Y. Qi, and J. Zhao, Layer-dependent magnetic phase diagram in $Fe_nGeTe_2 (3 \leqslant n \leqslant 7)$ ultrathin films, Commun. Phys. **5**, 140 (2022).

[75] C. Trainer, O. R. Armitage, H. Lane, L. C. Rhodes, E. Chan, I. Benedičič, J. A. Rodriguez-Rivera, O. Fabelo, C. Stock, and P. Wahl, Relating spin-polarized STM imaging and inelastic neutron scattering in the van der Waals ferromagnet $Fe_3GeTe_2$, Phys. Rev. B **106**, L081405 (2022).

[76] S. Bao, Y. Gao, J. Wang, S.-i. Yano, Y. Shangguan, Z. Huang, J. Liao, W. Wang, B. Zhang, S. Cheng, H. Xu, Z.-Y. Dong, S.-L. Yu, W. Li, J.-X. Li, and J. Wen, Magnon damping as a probe of Kondo coupling in magnetically ordered systems, Nat. Commun. **17**, 3557 (2026).

[77] X. Bai, F. Lechermann, Y. Liu, Y. Cheng, A. I. Kolesnikov, F. Ye, T. J. Williams, S. Chi, T. Hong, G. E. Granroth, A. F. May, and S. Calder, Antiferromagnetic fluctuations and orbital-selective Mott transition in the van der Waals ferromagnet $Fe_{3-x}GeTe_2$, Phys. Rev. B **106**, L180409 (2022).

[78] M. Corasaniti, R. Yang, K. Sen, K. Willa, M. Merz, A. A. Haghighirad, M. Le Tacon, and L. Degiorgi, Electronic correlations in the van der Waals ferromagnet $Fe_3GeTe_2$ revealed by its charge dynamics, Phys. Rev. B **102**, 161109(R) (2020).

[79] J. Liu, L. Zhou, S. Li, E. Zhao, and N. Tang, Anomalous temperature dependence of uniaxial magnetocrystalline anisotropy in the van der Waals ferromagnet $Fe_3GeTe_2$, Phys. Rev. B **109**, L060404 (2024).

[80] Z. Shu, S. Zhang, and T. Kong, Spin stiffness and spin excitation gap of van der Waals ferromagnetic $Fe_{3+\delta}GeTe_2$, J. Phys.: Condens. Matter **36**, 385801 (2024).

[81] V. Y. Verchenko, A. A. Tsirlin, A. V. Sobolev, I. A. Presniakov, and A. V. Shevelkov, Ferromagnetic order, strong magnetocrystalline anisotropy, and magnetocaloric effect in the layered telluride $Fe_{3-\delta}GeTe_2$, Inorg. Chem. **54**, 8598 (2015).

[82] S. Y. Park, D. S. Kim, Y. Liu, J. Hwang, Y. Kim, W. Kim, J.-Y. Kim, C. Petrovic, C. Hwang, S.-K. Mo, H.-j. Kim, B.-C. Min, H. C. Koo, J. Chang, C. Jang, J. W. Choi, and H. Ryu, Controlling the magnetic anisotropy of the van der Waals ferromagnet $Fe_3GeTe_2$ through hole doping, Nano Lett. **20**, 95 (2020).

[83] H. Ren and M. Lan, Progress and prospects in metallic $Fe_xGeTe_2 (3 \leqslant x \leqslant 7)$ ferromagnets, Molecules **28**, 7244 (2023).

[84] R. Roemer, D. H. D. Lee, S. Smit, X. Zhang, S. Godin, V. Hamza, T. Jian, J. Larkin, H. Shin, C. Liu, M. Michiardi, G. Levy, Z. Zhang, R. J. Green, C. Kim, D. Muller, A. Damascelli, M. J. Han, and K. Zou, Unraveling the electronic structure and magnetic transition evolution across monolayer, bilayer, and multilayer ferromagnetic $Fe_3GeTe_2$, npj 2D Mater. Appl. **8**, 63 (2024).

[85] H.-J. Deiseroth, K. Aleksandrov, C. Reiner, L. Kienle, and R. K. Kremer, $Fe_3GeTe_2$ and $Ni_3GeTe_2$ – Two new layered transition-metal compounds: Crystal structures, HRTEM investigations, and magnetic and electrical properties, Eur. J. Inorg. Chem. **2006**, 1561 (2006).

[86] H. Weerahennedige, Y. Karki, H. Aljeailan, H. Weerarathne, Z. Ronau, S. Dharmasena, S. E. Zeltmann, D. A. Muller, G. Sumanasekera, and J. B. Jasinski, Effect of limited Ni incorporation on the thermopower and Hall effect of layered $Fe_3GeTe_2$, J. Alloys Compd. **1080**, 190777 (2026).

[87] M. T. Johnson, P. J. H. Bloemen, F. J. A. d. Broeder, and J. J. d. Vries, Magnetic anisotropy in metallic multilayers, Rep. Prog. Phys. **59**, 1409 (1996).

[88] H. Williams, Magnetic properties of single crystals of silicon iron, Phys. Rev. **52**, 747 (1937).

[89] Y. Huang, N. Zuo, Z. Zhang, X. Xing, X. Yao, A. Zhang, H. Ma, C. Xu, W. Jiao, W. Zhou, R. Sankar, D. Qian, and X. Xu, In-plane magnetic anisotropy and large topological Hall effect in self-intercalated ferromagnet $Cr_{1.61}Te_2$, Adv. Funct. Mater. **36**, e10351 (2026).

[90] H. B. Tran, H. Momida, Y.I. Matsushita, K. Sato, Y. Makino, K. Shirai, and T. Oguchi, Effect of magnetocrystalline anisotropy on magnetocaloric properties of an $AlFe_2B_2$ compound, Phys. Rev. B **105**, 134402 (2022).